Precambrian Research 340 (2020) 105624

Contents lists available at ScienceDirect

Precambrian Research

journal homepage: www.elsevier.com/locate/precamres

Biogenesis of the Neoproterozoic kremydilite manganese ores from Urucum (Brazil) – A new manganese ore type

João Carlos Biondi[a,1], Márta Polgári[b,c,*,1], Ildikó Gyollai[b], Krisztián Fintor[d], Ivett Kovács[b], József Fekete[b], Stephen J. Mojzsis[b,e,*]

[a] Federal University of Paraná State, Polytechnic Center, Geology Department, 81531-980 Curitiba, Brazil
[b] Institute for Geological and Geochemical Research, RCAES, Hungarian, Academy of Sciences, 1112 Budapest, Budaörsi u. 45, Hungary
[c] Eszterházy Károly University, Dept. of Natural Geography and Geoinformatics, 3300 Eger, Leányka u. 6, Hungary
[d] Szeged University, Dept. of Mineralogy, Geochemistry and Petrology, 6722 Szeged, Egyetem u. 2-6, Hungary
[e] University of Colorado, Department of Geological Sciences, 2200 Colorado Avenue, UCB 399, Boulder, CO 80309-0399, United States

ARTICLE INFO

Keywords:
Urucum Ediacaran manganese deposit
Kremydilite
Microbialite
Enzymatic oxidation, cell and extracellular polymeric substance mineralization

ABSTRACT

The Urucum district in Mato Grosso do Sul (Brazil), hosts the youngest and largest sedimentary Mn ore of Neoproterozoic age; units Mn-1, Mn-2, and Mn-3 are found in jaspilites and ironstones, and represent approximately 600 Mt of extractable rock with 27–44% Mn and 12–30% Fe. High-resolution optical- and cathodoluminescence microscopy, as well as Raman and FTIR spectroscopy show that the lower Mn-1 is ferruginous, while the upper Mn-1 consists mainly of 30–75 vol% braunite, < 0.5% aegirine, 3–15% quartz, 5–10% feldspar, and 1–5% clay minerals, including apatite, chlorite, and organic matter. Here, we model the control of this ore mineralogy by homogeneous oxidation and microbial processes. Layers Mn-2 and Mn-3 contain *kremydilite*, as a characteristic ore structure, with 77–95 vol% cryptomelane, 0–23% hollandite, 9–19% braunite, 7–21% hematite, and 0–5% pores filled with clay minerals and organic matter. These are present within a micro-nodule matrix composed of cryptomelane and hematite in varying proportions. The first syngenetic products of microbial enzymatic oxidation were, on the Fe side, ferrihydrite and lepidocrocite, and on the Mn side, vernadite, todorokite, birnessite, and manganite. These formed under obligatory oxic (Mn) and suboxic (Fe) conditions and close to neutral pH. We describe the genesis of Urucum via complex diagenetic processes, which include the decomposition and mineralization of cellular- and extracellular-polymeric substances from Fe and Mn bacteria and cyanobacteria. The kremydilite forms in successive stages of oxidation of organic matter mediated by microbes, which generate pores and produce methane and CO_2/H_2 bubbles. They are a unique type of diagenetic structure formed by heterotrophic cell colonies randomly activated in the microbialite milieu following burial in suboxic neutral/alkaline conditions, side-by-side with the lithification and stabilization of the mineral assemblages.

Significance statement: The Neoproterozoic Urucum manganese deposit (Brazil) is a ~600 Mt microbially-mediated sedimentary Mn ore. Proto-ore formation via sedimentation and diagenesis occurred under suboxic-oxic and semi-neutral pH conditions in the Ediacaran ocean, wherein microbial Mn(II) oxidation ensued from the fine-grained accumulation of Mn oxides and organic matter. Oxic conditions that facilitated enzymatic Mn oxidation and overwhelmed microbial Fe oxidation appears as a sharp contact between manganese and iron beds. The Urucum deposit arose from a complex suite of diagenetic processes, including decomposition and mineralization of microbially-derived organic matter involving extracellular polymeric substances. *Kremydilite* – a new type of diagenetic concentric Mn mineral structure – formed by randomly activated heterotrophic cell colonies that generated pores in the microbialite sediment after burial, coincident with lithification.

* Corresponding authors at: Institute for Geological and Geochemical Research, RCAES, 1112 Budapest, Budaörsi str. 45, Hungary.
E-mail addresses: biondiufpr@gmail.com (J.C. Biondi), rodokrozit@gmail.com (M. Polgári), gyildi@gmail.com (I. Gyollai), iv.kovacs@gmail.com (I. Kovács), fekete.jozsef@csfk.mta.hu (J. Fekete), mojzsis@colorado.edu (S.J. Mojzsis).
[1] The first two authors contributed equally to this work.

https://doi.org/10.1016/j.precamres.2020.105624
Received 28 March 2019; Received in revised form 5 December 2019; Accepted 14 January 2020
Available online 21 January 2020

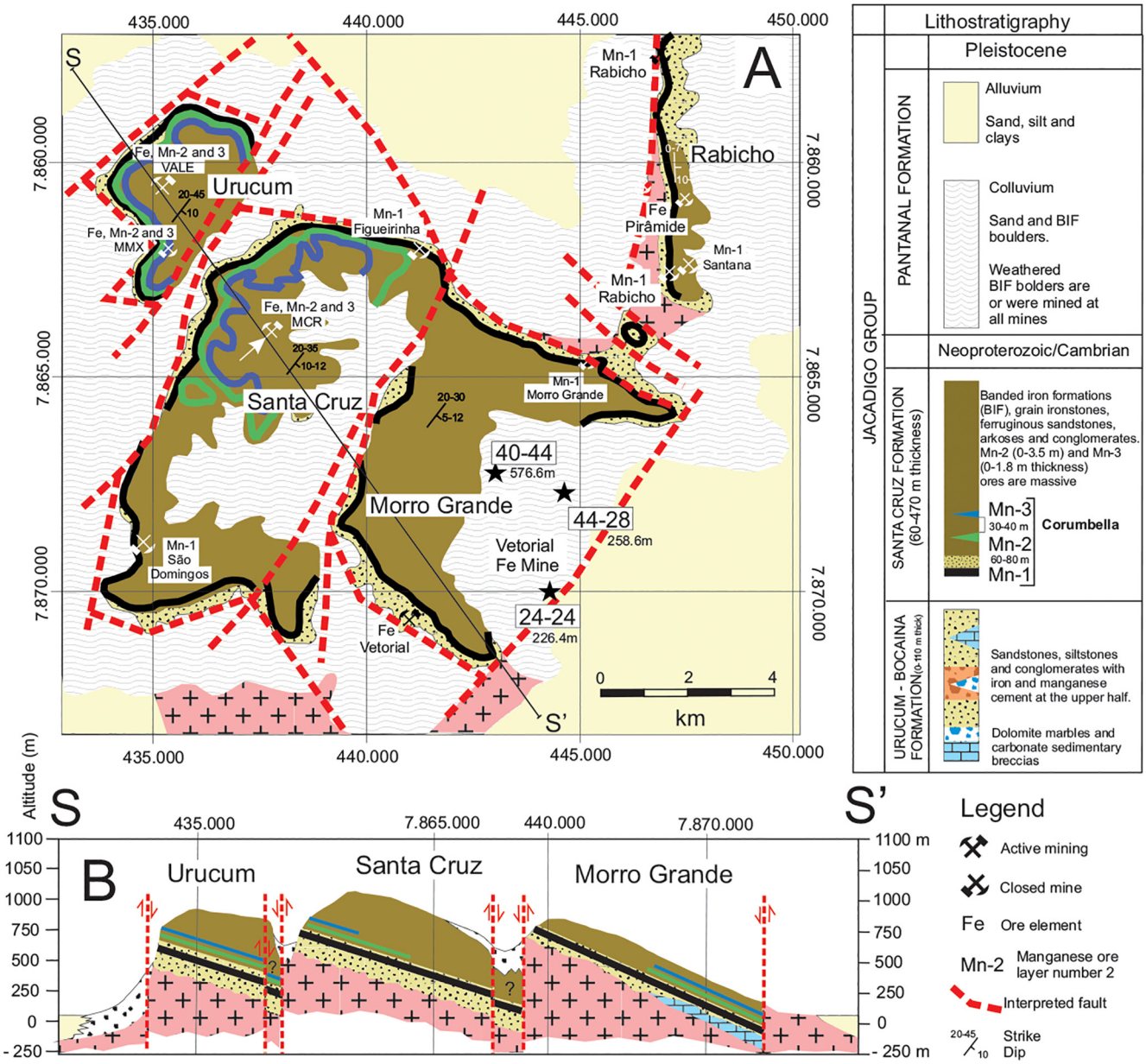

Fig. 1. (A) Map showing the positions of manganese layers Mn-1 to Mn-3 and the mines of the central Urucum region (modified after Urban et al. 1992, Biondi and Lopez, 2017) and, (B) S – S' regional geological section. The thicknesses of layers Mn-1 to Mn-3 are exaggerated by a factor of approximately ten. UTM coordinates referenced to Datum WGS 84. (For interpretation of the references to colour in this figure legend, the reader is referred to the web version of this article.)

1. Introduction

The Urucum mining district occupies an area of approximately 800 km^2 and is located in the Pantanal swamps region of west-central Brazil. Three layers of massive manganese oxides, named Mn-1, Mn-2, and Mn-3, occur interbedded with massive jasper, banded iron formations (BIFs), and massive iron formations (IF) that comprise the Santa Cruz Formation of the Neoproterozoic Jacadigo Group (Urban et al., 1992; Frei et al., 2017; Fig. 1 and SI 1-Fig). It was estimated that the Urucum district originally contained more than 600 Mt of rock with the manganese content between 27 and 44 wt% and iron content between 12 and 30 wt% (Urban et al., 1992).

The stratigraphic sequence of the Urucum region was first defined by Dorr (1945) and Almeida (1946), who also conducted the first systematic studies on the origin of iron and manganese deposits in the region. Urban et al. (1992) mapped the entire mining region, and since that time, the regional geological map has been minimally updated. Following the work of Urban et al. (1992), the most relevant changes to our understanding of the regional geology arose from the work of Freitas et al. (2011), who detailed the Jacadigo Group lithologies and defined their sedimentation environments. Biondi and Lopez (2017) identified faults that acted as conduits for hydrothermal fluids which altered the rocks of the Jacadigo Group basement, and exhaled fluids with iron and other elements at the base of the sedimentary sequence of the Urucum basin. They also correlated the Mn-1, Mn-2, and Mn-3 layers with those recognized at different Urucum sites.

Various and mutually-exclusive proposed genetic models for the Jacadigo Group iron and manganese rocks have been a topic of discussion and debate since their discovery. These models can be summarized as follows: (a) marine genesis with sediments of continental origin (Dorr, 1945); (b) marine genesis with sediments of marine origin (Almeida, 1946; Putzer, 1958; Haralyi and Walde, 1986); (c) volcanogenic marine genesis (Walde, 1981; Walde et al., 1981; Leonardos and Walde, 1982; O'Connor and Walde, 1985); (d) formation in a glacio-

marine sedimentary environment followed by supergene enrichment (Schneider, 1984; Schreck, 1984; van Leeuwen and Graaf, 1987; Graf et al., 1994; Costa et al., 2005); (e) sedimentary genesis in a flooded graben with a contribution of hydrothermal leaching from hidden mafic rocks (Haralyi and Walde, 1986; Walde, 1988; Trompette et al., 1998); (f) SEDEX, or sedimentary exhalation (Dardenne, 1998); and (g) sedimentary genesis in an oceanic environment with a deep-sea hydrothermal contribution (Klein and Ladeira, 2004). Recently, Angerer et al. (2016) proposed a biologically-mediated origin in a glacio-marine environment for the carbonate BIFs of the Santa Cruz Mine region located on the southeastern part of the Santa Cruz plateau. In a recent comprehensive study, Biondi and Lopez (2017) (a) recognized the biogenic mediation during the genesis of manganese ore; (b) described in detail mineral structures termed by them *kremydilites* and argued that they may represent fossilized microbial colonies from organisms that mediated the formation of the manganese layers; and (c) modified the region's stratigraphy based on the fossil assemblages, showing that the Urucum iron-manganese rocks correlate to the carbonate rocks of the Bocaina Formation, of the Corumbá Group, previously considered post-depositional to those of the Jacadigo Group.

The Ediacaran Period of formation is proposed by the authors based on the presence of the *Corumbella Verneri* fossil, found amidst the ironstones separating Mn-2 from Mn-3 (Fig. 2B and Fig. 4B to D in Biondi and Lopez, 2017). This fossil has always been considered Ediacaran, which establishes a wider interest concerning the Urucum Mn deposit.

Here, we explore the origin of kremydilites described in Biondi and Lopez (2017) and present a model that explains the processes of sedimentation and diagenesis that facilitated the origin of these structures and the manganese layers. Recent works have provided a geological setting diagram, mineralogy (low magnification optical microscopy, X-ray diffraction, SEM-EDS-based), and chemistry datasets based on bulk samples and *in situ* (SEM-EDS) data (e.g. Frei et al., 2017), but microbial mediation as a plausible mechanism for the genesis of these rocks is still under debate (Biondi and Lopez, 2017). We expand the results of these previous studies with more detailed optical microscopy (OM), cathodoluminescence microscopy (CL), Raman- and Fourier-transform infrared spectroscopy (FTIR) to document the micro-mineralogy, presence, and distribution of embedded organic matter. The goal here is to explore the role of microorganisms in the process of manganese ore genesis from Urucum, and to understand the diagenesis, structures, and process of formation of kremydilites.

2. Geological and geochronological background

The Santa Cruz Formation is mainly composed of jaspilitic BIFs, (massive) iron formations (IFs), massive banded jasper, and ferruginous arkosic silt and sandstones. The greatest thickness of the Santa Cruz Formation, 396 m, is documented in drill hole (DH) 44–28, made at the Vetorial Mine, and bookended by a 40 m section at the northern end of the Rabicho plateau (Fig. 2). The massive manganese layers, Mn-1, Mn-2, and Mn-3, occur in the lower half of this formation and are interlayered with BIFs and massive jasper.

The Jacadigo and Corumbá Groups are considered coeval (Biondi and Lopez, 2017) and of Ediacaran age, based on the presence of stromatolites below Mn-1 (Jacadigo Group) and *Corumbella* fossils in the rocks of the Bocaina and Santa Cruz Formations (respectively, Corumbá and Jacadigo Groups). The age of this fossil in the ironstones of the Santa Cruz Formations (Jacadigo Group) and limestones of the Tamengo Formation (Corumbá Group) was estimated at ca. 550 Ma (Germs, 1972; Grant, 1990; Grotzinzer et al., 1990; Hofmann and Mountjoy, 2001; Bengtson, 2002). The proposed age of this horizon was 555–542 Ma by ichnofossils, identified by Parry et al. (2017), in the Bocaina Formation. These ages are consistent with U-Pb geochronology of detrital zircons from a volcanic ash layer intercalated with carbonate rocks of the Tamengo Formation, at 543 ± 3 Ma (Babinski et al., 2008), and the $^{40}Ar/^{39}Ar$ age of 587 ± 7 Ma for cryptomelane in the Mn-1 to Mn-3 layers (Piacentini et al., 2013; Frei et al., 2017 and references therein).

Dating braunite from the Mn-1 layer, Piacentini et al. (2013) interpreted the 547 ± 3 to 513 ± 4 Ma ($^{40}Ar/^{39}Ar$) age as a minimum age, arguing that the Ar/Ar thermo-chronological system was rejuvenated by tectonic warming, which was considered a consequence of the metamorphism underwent by the Jacadigo Group rocks. Also using the $^{40}Ar/^{39}Ar$ method, they dated 513 ± 3 Ma some crystals of muscovite collected from the arkoses that are interlayered with the BIFs, which was also considered metamorphic. According to Piacentini et al. (2013), these ages are "*possibly related to disruption between the Amazon Craton and the Apa River cratonic fragment and they do not reflect the time of Jacadigo Group deposition*", which would be greater than 590 Ma, and concluded that Jacadigo's rocks would have at least 587 ± 7 Ma.

To reconstruct the paleogeography of the sedimentary basin, Mn-2 and Mn-3 were leveled and used as stratigraphic markers. This procedure makes it possible to outline the geometrical differences between the Mn-layers. This reconstruction shows that stratigraphy observed within the Urucum plateaux always includes Mn-1, and that this stratum lines the basin floor wherever the Jacadigo Group is described (e.g., Urban et al., 1992; Biondi and Lopez, 2017) (Fig. 2). Yet, unlike Mn-1, both the Mn-2 and Mn-3 layers occur only in the interpreted depocenter of the basin, in the region of Urucum, Santa Cruz and southeast of the Morro Grande plateaux (Fig. 1). In the interior of each plateau, mining of the manganese layers reveals that Mn-2 and Mn-3 are flat and parallel to one another, whereas the Mn-1 unit follows the contours of the basin floor. By positioning Mn-2 and Mn-3 in their respective stratigraphic horizons it is now possible to reconstruct Urucum marginal basin floor (Fig. 2).

The origin of the sediments of Urucum has been detailed elsewhere (Walde, 1981; Walde et al., 1981; Leonardos and Walde, 1982; O'Connor and Walde, 1985; Haralyi and Walde, 1986; Walde, 1988; Trompette et al., 1998, Dardenne, 1998, Klein and Ladeira, 2004, Angerer et al., 2016; Biondi and Lopez, 2017), and we provided a brief synopsis, here. The Santa Cruz Formation formed as an in-fill of an ancient graben with iron and manganese-rich sediments overlying fluvial deposits from the Urucum Formation, while limestones from the Bocaina and Tamengo Formations were deposited in the shallow marginal regions (Biondi and Lopez, 2017; Fig. 2). As has been proposed for some Phanerozoic Mn ores (e.g. Polgári et al., 2012a,2012b,2016b), the most probable sources of the Mn and Fe was hydrothermal exhalations in a submarine environment. The Mn and Fe fluids were transported to the sedimentary basin via basement faults (SI 1–2-Figs) that became activated each time the graben widened. During inundations attributed to sedimentation of the Mn-1, Mn-2, and Mn-3 units, Mn and Fe discharged on basin floor mixed with Mn and Fe brought in by water from the open ocean as well as with that originating from the exhalates located outside the Urucum basin.

A transition between the Urucum and Santa Cruz formations through the Mn-1 horizon exists in all mines from the area (Urban et al., 1992). Furthermore, Biondi and Lopez (2017) showed that there are typically two or more layers of Mn-1 manganese ore with meter- to decimeter-scale thicknesses, locally interlayered with jaspillite-rich clasts. We now describe these relationships in more detail.

The lower Mn-1 ore layer is relatively siliceous and composed mainly of braunite, cryptomelane cement and Mn–Fe-rich carbonate, whereas the Upper Mn-1 layer is a fine-grained, massive, clastic layer of manganese oxides with undulating parallel lamination and numerous decimeter-scale oblate structures, characterized by a massive core and silty clay and arkose wrap dubbed amygdalites (Fig. 3C). The ore layer is bounded by sharp planar contacts typically overlain by conglomerate consisting of angular granite pebbles in an arkosic matrix. Layers Mn-2 and Mn-3 contain mostly massive manganese ore with lamination. They are composed mainly of cryptocrystalline manganese oxides and hydroxides, commonly containing kremydilites (Fig. 3D-E and 4) with minor amygdalites (Biondi and Lopez, 2017). In Mn-2 and Mn-3, what

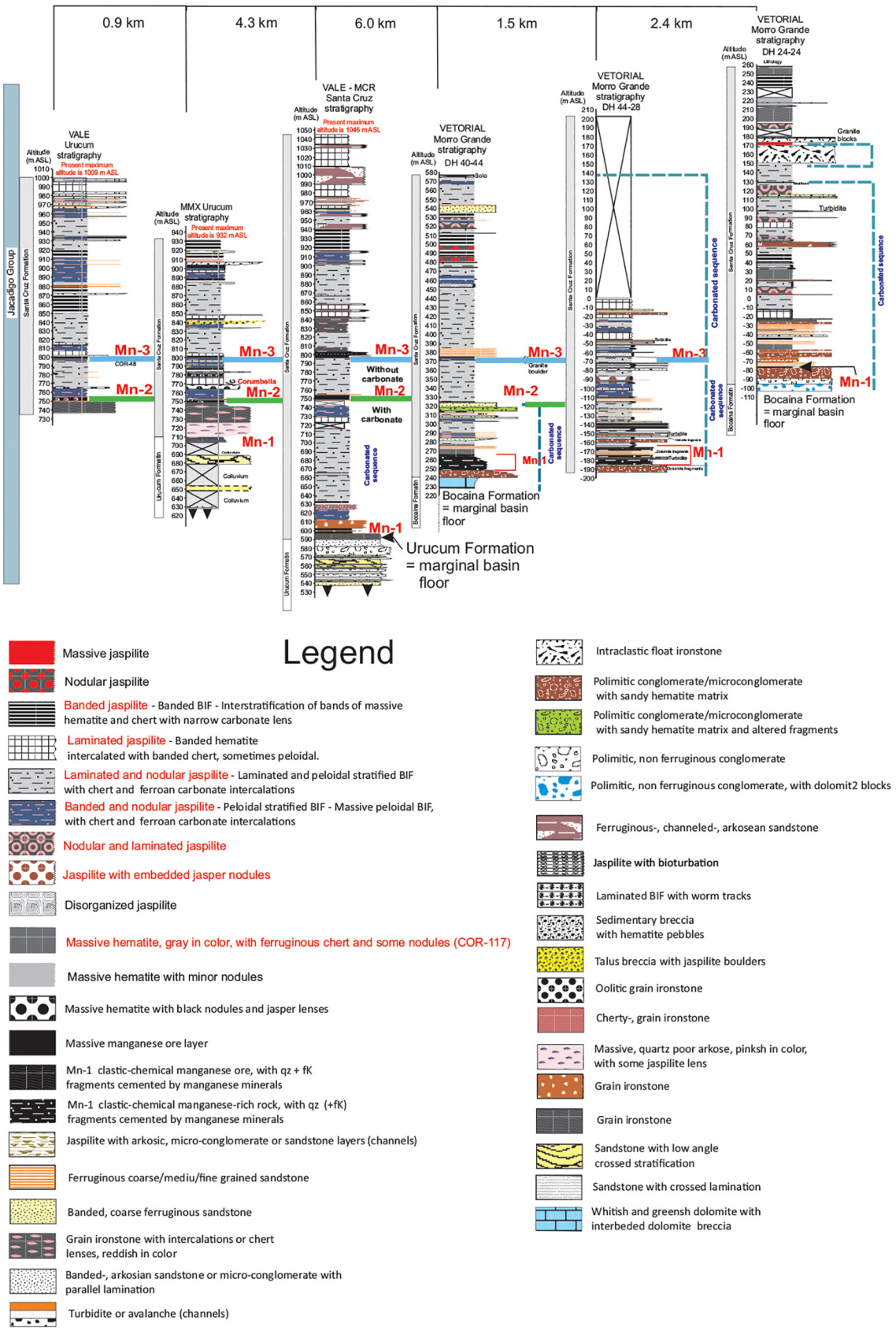

Fig. 2. Stratigraphic columns made in the region of manganese and iron mines of Urucum, and sample locations. Note that the Mn-1 layer is not flat, and its shape is adapted to the basin floor while Mn-2 and Mn-3 are plane-parallel (modified after Urban et al. 1992, Biondi and Lopez, 2017). (For interpretation of the references to colour in this figure legend, the reader is referred to the web version of this article.)

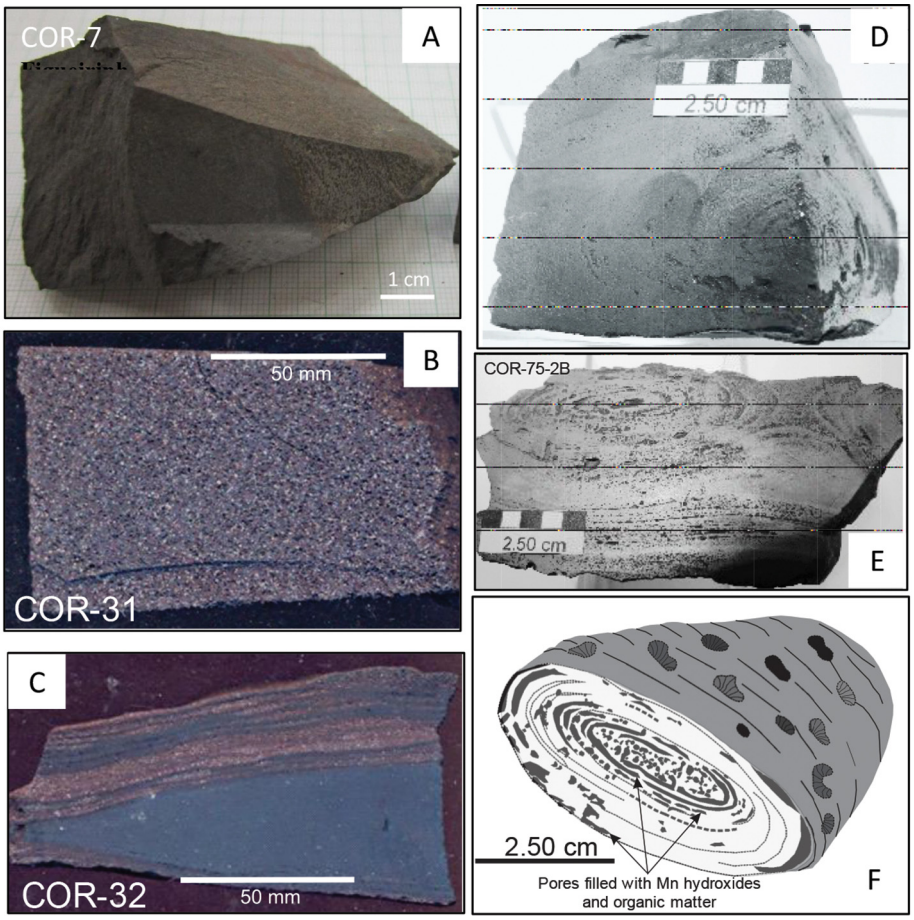

Fig. 3. Representative samples of Mn-1 (A-C), Mn-2, and Mn-3 (D-F). (A) Sample of silt, massive Mn-1 (fragments of quartz, altered feldspar, apatite, chert). (B) Clast-bearing, massive-, arkosean-, Fe-rich sample from Lower Mn-1. (C) Oblate amygdalite-bearing massive, fine-grained manganese ore, with arkosean Fe-rich bands. (D-F) Kremydilite in its most developed form after diagenesis, sawed according to orthogonal planes, showing its oblate form. (D) Kremydilite sawn according to orthogonal planes, showing its oblate form. (E) The concentric organization of the several layers that constitute complex kremydilite, each concentric layer with limits marked by pores. (F) Schematic drawing of a cut kremydilite, illustrating its shape and its interior. For more representative samples see SI 3-Fig. (For a colour in this figure, the reader is referred to the web version of the article.)

have been interpreted as the remains of microbial colonies form oblate, 5–15-cm sized concentric kremydilite structures, within the fine-grained and biomass-rich basin floor shale as well as intergranular, oblate gas structures (Fig. 4A, C, F, and H). The main features of the ore beds, including their mineralogical and selective element compositions are summarized in Table 1.

The textures of the Mn-2 and Mn-3 layers express as 1–10 mm-sized spherical, often zoned manganese oxide micro-nodules that coalesce to form the massive ores. These probably involved the aforementioned kremydilite structures made solely of manganese and minor iron oxides. All observed Mn-2 and Mn-3 outcrops have kremydilites, although they do not constitute all of the ore mass from these layers. As previously described, kremydilites occur between the ore bands (Fig. 4A–J), which are massive or banded (and/or laminated), and are distributed in the layers in an apparently homogeneous manner. It is difficult to estimate the volume occupied by kremydilites owing to the fact that they are complicated to see in discontinuous outcrops. For those observed on the mining fronts, it is likely that they occupy more than about 50% of the ore layer by volume.

2.1. Forms and type of kremydilites

Kremydilites occur only between the laminations of the massive ore in the Mn-2 and Mn-3 layers, and are absent in banded- or massive ironstones. They are always contoured by the fine laminated ore with micronodular, microbialite micro-texture, in which the diameters of micro-nodules range from 0.2 to 0.8 mm (Fig. 4; SI 5-Fig, zones 1, 2, 3; and zones 20 to 24). Microbialite and micro-nodule rich layers are in turn contoured by wavy microbialite layers apparently composed by the amalgamation of nodules smaller than 10 μm. Its forms are oblate, centimeter-to-decimeter scale (Fig. 3) and concentrically zoned. Structures of what we interpret to be the different growth development stages also appear to occur together (Figs. 4 and 5), and each stage of growth is marked by the presence of pores, which delineate coarse concentric, sometimes incomplete envelopes (Fig. 4). Kremydilites on the other hand are porous structures absent of micro-nodules. They occur in varied forms as shown in Fig. 4A to H.

The simplest kremydilite form consists of a bubble-filled nucleus (Fig. 4A), followed by those with a nucleus having diffuse borders (Fig. 4C). Other forms include a nucleus with one (Fig. 4E) or two (Fig. 4G) diffuse concentric laminae (or shells). The more complex kremdylites, with a nucleus and many concentric shells delineated by millimeter to submillimeter pores, crosscut with lighter, massive, and metallic zones (Fig. 4I). In general, the various kremydilite forms contain many oblate structures (Fig. 4A, E, and G). These are less than 20 mm across distributed along the layer containing the kremydilite, and inside and/or near them. Mesoscopic inspections of sawn samples (Fig. 4K) as well as thin and polished sections, show that each layer contains disseminated pores. The quantity of pores increases toward the margin of the shell, and each lamina is surrounded and delimited by areas with high pore density (Biondi and Lopez, 2017).

The pores are often lined by shiny acicular microcrystals of cryptomelane and/or contain organic matter (Biondi and Lopez, 2017). Although kremydilites do not contain micro-nodules, and are instead inside the micronodular bands and contoured by microbialite layers, the outermost zones of kremydilite appear to have a composition similar to that of amalgamated micro-nodules. In these zones, the presence of ring-like structures of carbonate microcrystals are common (SI 5-Fig, zone 16 - detail image, Biondi and Lopez, 2017). The zones closer to the nucleus (zones 9, 10, and 11) contain mixed anhedral minerals with metallic luster, but with larger dimensions than the anterior zones. The nucleus of the kremydilites (zones 12 and 13) are microgranular

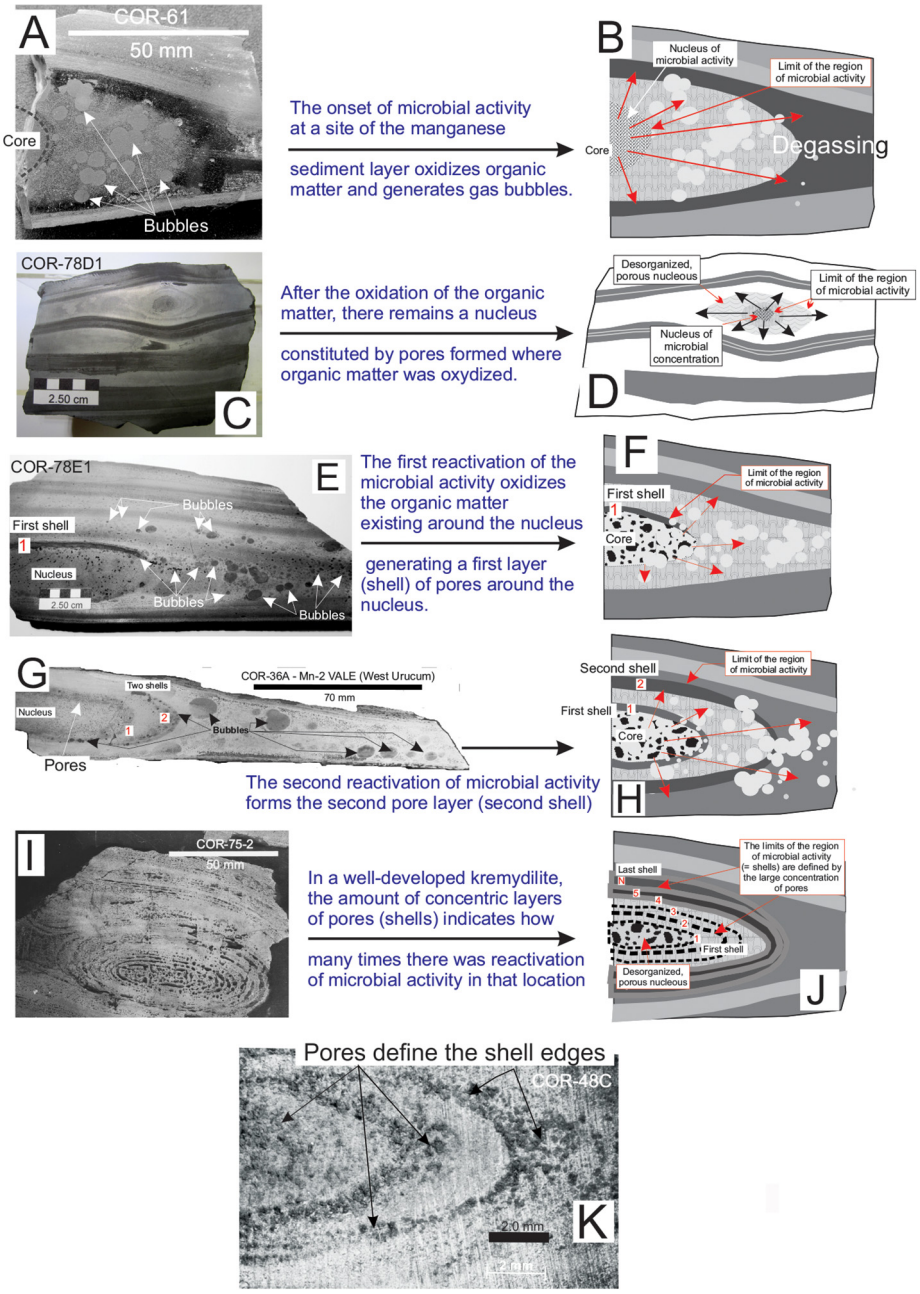

Fig. 4. Different stages of development or growth of kremydilites. The text in the figure explains each stage. Bubbles: oblate structures. (A-I): photos of polished surfaces, (K) photomicrograph. (For colour symbols used in this figure, the reader is referred to the web version of this article.)

and heterogeneous.

3. Samples

Representative samples and the methods applied (number of photos and spectra) are summarized in Table 2 and Figs. 3 and 4. Localities of the sample collection are shown in Fig. 2.

The samples of Mn-1 are (Fig. 3, SI 3-Fig): COR-4B, a clast-bearing massive ironstone; COR-6, a massive manganese ore; COR-7, a very fine-grained clast-bearing ore with braunite and carbonate; COR-10, a sandy, detritic ore with braunite, quartz, and feldspar; COR-31, an arkosic sandstone with hematite matrix; and COR-32, an amygdalite with cryptomelane massive nucleus surrounded by arkosic sandstone with hematite matrix.

Samples of Mn-2 and Mn-3 are: COR-81, a sample of massive manganese ore; COR-78-F3 (Fig. 4F), a nucleus of porous kremydilite with diffuse boundaries, surrounded by two zones also with diffuse boundaries; COR-78-D1 (Fig. 4C), a kremydilite with a diffuse core enveloped by two shells, also with diffuse boundaries; COR-75-B5 (Fig. 4E), a porous kremydilite nucleus; COR-75-2 and COR-48 (Fig. 4J), complex kremydilites with porous core surrounded by many concentric, porous shells; and COR-36-A1 (Fig. 4G), a kremydilite with a nucleus and at least two shells (hereafter the samples are cited without COR).

4. Methods

Thin section and polished section mineralogy was described and quantified using a ZEISS Axio Imager A2m microscope (Federal University of Paraná State, Polytechnic Center, Geology Department, Curitiba, Brazil).

Petrographic structural-textural studies by optical rock microscopy

Table 1
Main features, mineralogical and selective element composition of ore beds (12 samples) (Biondi and Lopez, 2017).

Ore bed	Mn-1	Mn-2–3
Main features	Sandy (fragments of quartz, altered feldspar, apatite, chert), laminated, amygdalite-bearing	Kremydilite
Mineralogy	*Figueirinha-Upper Mn-1* 30–75 v% braunite < 0.5 vol% aegirine 3–15 vol% quartz 5–15 vol% feldspar 1–5 vol% clay minerals, apatite, chlorite locally 10–30 vol%Fe-dolomite or siderite, Mn-dolomite *São Domingos-Upper Mn-1* (laminated, amygdalite-bearing) 40–75 vol% cryptomelane-hollandite 10–30 vol% quartz 10–15 vol% hematite, apatite, clay minerals *Composition of amygdalite cores* 60–90 vol% cryptomelane (hollandite?) 0–10 vol% quartz 5–15 vol% hematite, clay minerals Santa Cruz-Mn-1 arkozic sandstone cemented by hollandite (cryptomelane, pyrolusite), quartz, feldspar, hematite *Composition of ferruginous sandstone* 30–40 vol% hematite 60–70 vol% quartz 1–5 vol% clay minerals	77–98 vol% cryptomelane 0–23 vol% hollandite 9–19 vol% braunite 7–21 vol% hematite 0–5 vol% clay minerals and CM
Average chemical composition of selective elements (wt. %)		
Mn	Mn-1 contains a Lower and an Upper part, whose compositions vary locally, which is the reason why it is not possible to determine the average chemical composition of this unit.	50.06 (SD-2.73%)
Fe		8.58 (SD-2.59%)
K		1.82 (SD-0.75%)
Ba		0.29 (SD-0.30%)
LOI		10.80 (SD-0.88%)

Samples COR-16P, 16M, 17, 36A, 42, 43, 48L, 48P, 61L, 61P, 75 and 78 published in Biondi and Lopez (2017).

(OM) were also made on 12 thin sections in transmitted and reflected light (NIKON ECLIPSE 600 rock microscope, Institute for Geology and Geochemistry, Research Centre for Astronomy and Earth Sciences, Hungarian Academy of Sciences – IGGR RCAES HAS, Budapest, Hungary).

Cathodoluminescence (CL) petrography was carried out on 7 thin sections using a Reliotron cold cathode cathodoluminescence apparatus mounted on a BX-43 Olympus polarization microscope (Szeged University, Hungary). The accelerating voltage was 7–7.7 keV during the analysis. Cathodoluminescence spectra were recorded by using an Ocean Optics USB2000 + VIS-NIR spectrometer. Spectrometer specifications are a wavelength range of 350–1000 nm and 1.5-nm (FWHM) optical resolution.

Mineralogical analyses were performed on three bulk samples using a Rigaku Miniflex-600 X-ray diffractometer (XRD), with carbon monochromator and Cu-Kα radiation, at 40 kV and 15 mA (IGGR RCAES HAS, Budapest, Hungary). Mineral composition was determined on randomly oriented powdered samples. The diffraction patterns were processed using Siroquant V4 software, and the modal contents determined by the Rietveld method.

In situ FTIR microspectrometry used for micro-mineralogy and organic material identification on nine thin sections to determine the mineralogy and characterize the organic material, as well as clarify the concentric structures (415 spectra, IGGR RCAES HAS, Budapest, Hungary), using a Bruker FTIR VERTEX 70 equipped with a Bruker HYPERION 2000 microscope with a 20x ATR objective and MCT-A detector. During attenuated total reflectance Fourier transform infrared spectroscopy (ATR) analysis, the samples were contacted with a Ge crystal (0.5-μm) tip with 1 N pressure. The measurement was conducted for 32 s in the 600–4000 cm^{-1} range with 4-cm^{-1} resolution. Opus 5.5 software was used to evaluate the data. The equipment inappropriate for most of Mn-oxide determinations because those peaks fall in the < 600 cm^{-1} range (not equipped with that detector). Contamination by epoxy glue and glass was corrected for.

High-resolution *in situ* micro-Raman spectroscopy was used for micro-mineralogy and CM identification and distribution on 9 thin sections (1 polished section) (Szeged University, Hungary). A Thermo Scientific DXR Raman Microscope was used, with a 532-nm (green) diode pumped solid-state (DPSS) Nd-YAG laser, using 1.5-mW laser power and 50x objective lens in confocal mode (confocal aperture 25 μm slit). The acquisition time was 1 min, and the spectral resolution was ~2 cm^{-1} for each measurement. The distance between each point was 10 μm, and the measurement time was 10 min. A composite image

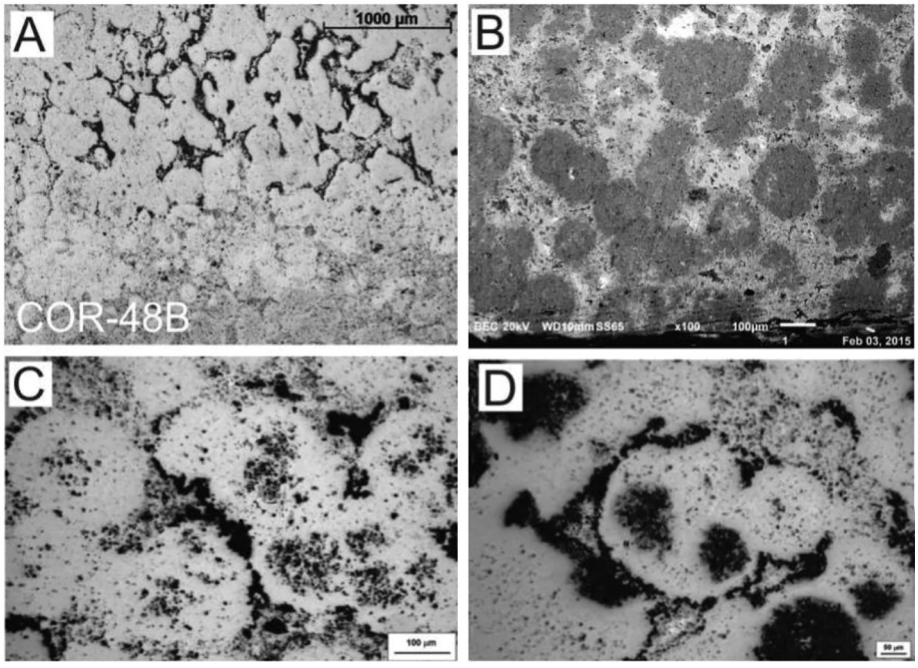

Fig. 5. Photomicrographs (reflected light) of the micro-nodules that constitute the massive parts of the Mn-2 and Mn-3 ore beds. (A-B) The larger nodules, < 0.8 mm (3A) at present are formed mainly by cryptomelane and hollandite, and the matrix is hematite (Biondi and Lopez, 2017). (C-D) Most micro-nodules are zoned, with a dark, porous nucleus. A, C, D photos are photomicrographs made by optical rock microscope, reflective mode, (B) is back scattered electron image by EPMA.

Table 2
Samples and used methods.

Sample ID	Layer	Locality (Fig. 1)	TS*	OM	CL	FTIR	Raman	XRD
COR-81	Mn-3	MCR-VALE mine, Sta Cruz Plateau	x	x(34)			x(1,903)	
COR-78-F3	Mn-2	Urucum-VALE mine, Urucum W plateau	x	x(65)		x(60)		
COR-78-D1	Mn-2	Urucum-VALE mine, Urucum W plateau	x	x(59)	x(11)		x(3,456)	
COR-75-B5	Mn-2	Urucum-VALE mine, Urucum W plateau	x	x(63)	x(6)		x(2,449)	
COR-75–2	Mn-2	Urucum-VALE mine, Urucum W plateau	x	x(56)	x(9)		x(1,209)	
COR-48B	Mn-2		x			x(1 7 8)		
COR-36-A1-A2	Mn-2	MMX mine, Urucum E plateau	x	x(56)		x(50)		
COR-10	Mn-1	Figueirinha mine, Sta Cruz N plateau	x	x(95)	x(23)	x(14)	x(5 0 4)	x
COR-7	Mn-1	Figueirinha mine, Sta Cruz N plateau	x	x(38)	x(27)	x(12)	x(5 0 4)	x
COR-6	Mn-1	Figueirinha mine, Sta Cruz N plateau	x	x(46)		x(37)		
COR-4B	Mn-1	Figueirinha mine, Sta Cruz N plateau	x	x(43)	x(10)		x(4 0 0)	
COR-32	Mn-1	Sao Domingos mine, Sta Cruz SW plateau	x	x(79)		x(32)		
COR-31	Mn-1	Sao Domingos mine, Sta Cruz SW plateau	x	x(56)	x(27)	x(32)	x(5 0 4)	x
Total 14 samples (photos, spectra)				690	113	415	10,997	3

Abbrev.: TS-thin section; OM-optical rock microscopy; CL-cathodoluminescence microscopy; FTIR-ATR-infra red spectroscopy; Raman-Raman spectroscopy; XRD-X-ray powder diffraction gray background: samples from Mn-2 and 3 beds (Figs. 3-4 and SI 3-Fig) number of analyses in brackets.

of thin sections of Raman microscopy measurements and a series of Raman spectra acquired along the vertical sections are provided in the thin section photomicrographs (arrow points to measurement direction). Diagrams are organized in terms of peak height versus analytical spot number for each of the phases along the Raman-scanned section. Intensities were normalized to the highest peak for each spectrum.

Raman measurements were taken on 9 samples (4B, 7, 10, 31, 36-A, 75–2, 75-B5, 48-D1, 81). In the case of the homogeneous-like cases 400–500 and in the case of 75–2, 800 spectra were taken along the line shown on section photos (4B, 7, 10, 31). These are systematic investigations along the line profile. Spectra were obtained every 10 μm, providing a high-resolution sensitive study. In samples 75-B5, 78-D1, and 81, the measurements were taken across whole thin sections. The spectra were elaborated in two ways:

(1) Diagrams were organized in terms of peak height versus analytical spot number of each of the phases along the Raman scanned section (main minerals and organic matter in general). (2) A detailed determination of all spectra were also made. These results are summarized in tables (Excel files, numbers 1, 2, and 3 indicate the intensity—1-weak, 2-moderate, 3-strong—reference data on detection), in which the mineral composition can be followed from point to point, as well as the type of organic matter (Supporting Information).

Aside from the profile analyses, descriptions of the mineral phase transitions were also constructed for clarification of aegirine (5 photos, 4 mineral spectra, and 1 profile), braunite (3 photos, 10 point analyses, and 1 profile across mineral transitional zones), cryptomelane (18 photos, 54 point analyses, and 2 profiles across spheres), and the composition of the oblate structures (28 photos, 93 point analyses, and 1 profile).

The following Raman bands were used for normalization: rhodochrosite: ~1086 cm^{-1}, dolomite: ~1093–96 cm^{-1}, apatite: ~965 cm^{-1}, quartz: ~463 cm^{-1}; todorokite 633 cm^{-1}; manjiorite 641 cm^{-1}; ramsdellite: 650 cm^{-1}; cryptomelane: 183 cm^{-1} and 580 cm^{-1}; hollandite: 585 cm^{-1}; birnessite: 656 cm^{-1}; ferrihydrite: 707 and 1045 cm^{-1}; goethite: 297 and 385 cm^{-1}; celadonite: 545 cm^{-1}; barite: 446 and 985 cm^{-1}; johannite: 785 cm^{-1}; aegirine: 970 cm^{-1}; jacobsite: 620 cm^{-1}; hausmannite: 661 cm^{-1}; braunite: 210, 510, 685 cm^{-1}; and carbonaceous matter: ~1605 cm^{-1}. The identification of minerals was made with the RRUFF Database (Database of Raman – spectroscopy, X-ray diffraction, and chemistry of minerals: http://rruff.info/). Contamination by epoxy glue was taken into consideration. Along with the profile analyses, a detailed determination of all peaks was also made.

Comparing the two *in situ* methods, the AT-FTIR, which did not considerably modify the mineral phases while using the lowest exciting energy, was used to investigate the upper 1–2 μm of the samples. This is the also best method to determine organic matter (Polgári and Gyollai, 2019; Polgári et al., 2019). On the contrary, Raman spectroscopy, using higher excitation energy, often caused the transformation of metastable minerals to more stable phases. This method yielded information from the upper 3–4-μm depth of the sample surfaces and was the best method for identifying Mn oxides and hydroxides. The Raman comparative spectra database is more extensive than the AT-FTIR database.

5. Results

5.1. Optical (OM) and cathodoluminescence (CL) rock microscopy

5.1.1. Optical rock microscopy

Thin sections represent mineralized biomats based on structural observations, which are eminently visible on smaller magnification photos (40×) (Fig. 6, SI 6-, 7-Figs). In all thin sections, adequately high-resolution optical rock microscopy (1000×) supports a series of mineralized biomat microstructures, mineralized microbially produced textures (MMPT) as main constituents (Fig. 6, SI 8-Fig). This microbial microtexture is a basic feature of all the samples, in transmitted as well as reflective light. Well-preserved and mineralized remains of diverse filaments with pearl necklace-like, vermiform inner signatures, and coccoid-like forms embedded in the Mn ore beds are seen, and the whole samples appear densely woven. The minerals are very fine-grained (0.5–1 μm) except Mn-1, where clastic contribution occurs. The diameter of the mineralized filaments is around 0.5–1 μm, with variable length (Fig. 6).

Samples 4B, 7, 10, 31, 32 (all from Mn-1) include debris-like components of variable size (20–200 μm). In sample 4B, it seems that the darker gray mineral grains transform to lighter phase (SI 8-Fig). The debris grains are mainly quartz with few fragments of jasper and hydrothermally altered feldspar.

5.1.2. Cathodoluminescence microscopy

Cathodoluminescence revealed that a part of the debris-like grains (clastic components) is probably composed of real clasts showing the bright, characteristic CL of the mineral (e.g., quartz-blue, feldspar-yellowish) (Fig. 7AB, SI 9-Fig). Some other grains with sizes of some tens of μm resemble clasts but do not show luminescence. These non-luminescent grains are most probably secondary minerals formed via diagenesis (Marshall, 1998; Hassouta et al., 1999).

Bright blue luminescence is characteristic of kaolinite group-dickite (supported by Raman spectroscopy; Götze et al., 2002), which occurred frequently in our samples (samples 4B, 7, 10, 31, Fig. 7A, B, G, H). The numerous small or larger bright yellow minerals are apatite grains, which often have a lighter margin. These apatites occur along the ore

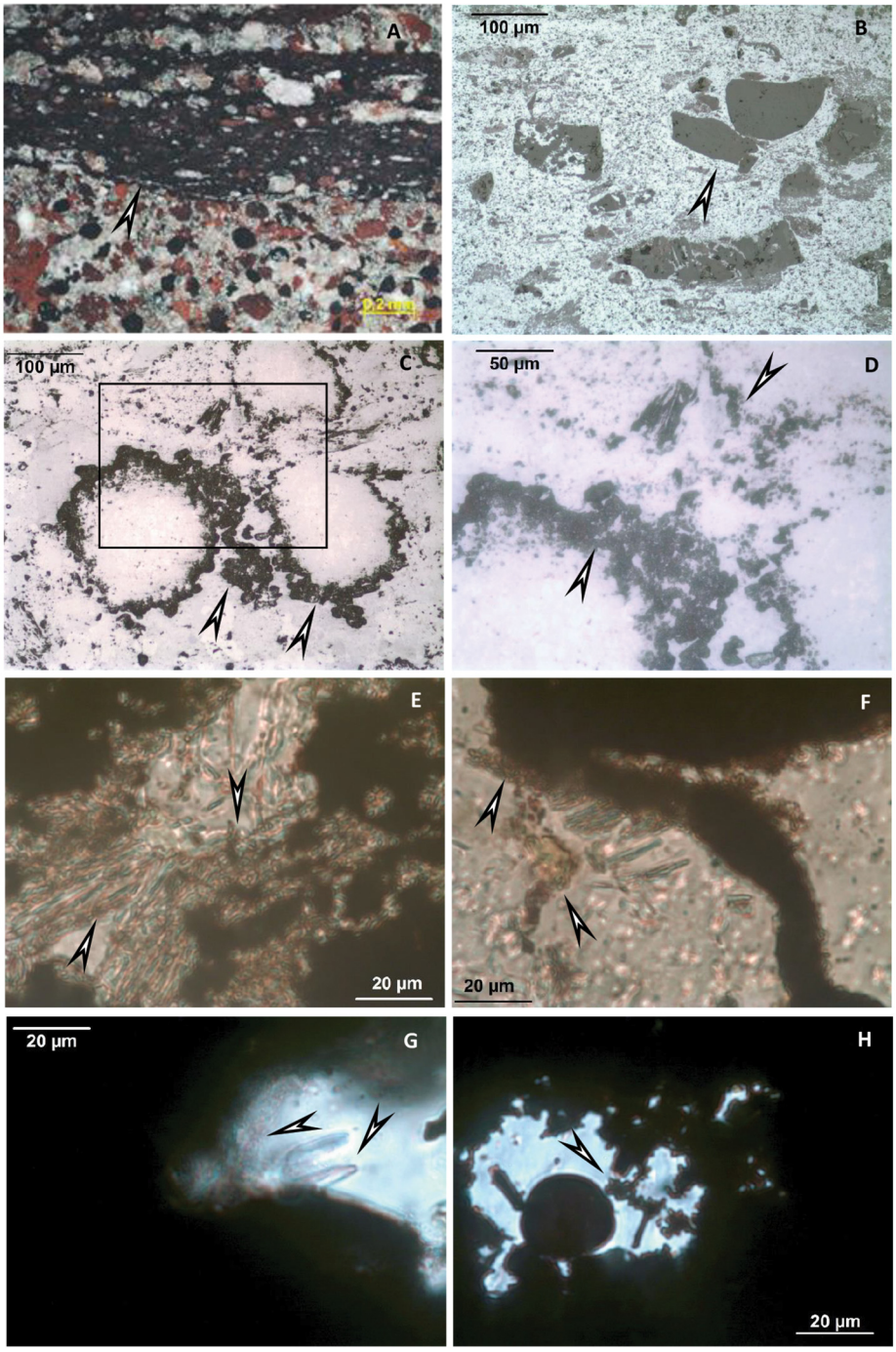

Fig. 6. Micro-textural features of samples (photomicrographs). Mineralized microbial biosignatures. (A) biomat (arrow, sample 36-A); (B) clastic particles (arrow, reflected light 1 N, sample 4B); (C) mineralized microbial biosignatures (arrows, reflected light 1 N, sample 75–2, rectangle shows enlarged area); (D) mineralized microbial biosignatures (arrows, reflected light 1 N, sample 75–2, enlarged area on C); (E) mineralized microbial biosignatures (arrows, 1 N, transmitted light, sample 7); (F) mineralized microbial biosignatures (arrows, reflected light 1 N, sample 10); (G, H) mineralized microbial biosignatures (arrows, 1 N, transmitted light, samples 32 and 36-A1). On (G) putative cyanobacteria are shown by arrow (based on similarity published by Gyollai et al., 2015 on Namibian Neoproterozoic sample). (For a colour in this figure, the reader is referred to the web version of the article.)

lenses, minerals, and laminae in a woven-like fine-grained biomat-type matrix which mark the borders as accompanying a series of minerals that occurred frequently (Fig. 7, SI 9-Fig) (samples 4B, 7, 10). The fine-grained rhodochrosite (mixed carbonate) show dull reddish (orange) luminescence (Fig. 7A, B) (samples 4B, 7, 10). Samples 75-2, 75-B5, and 78-D1 are non-luminescent.

5.2. FTIR spectroscopy

Measurements were performed in two ways: (i) randomly, in seven sections (6, 7, 10, 31, 32, 36-A1, 78-F3) and (ii) along profiles, in kremydilite sample 48B (Fig. 4K) and in oblate structure (36-A2) (Fig. 4H).

5.2.1. Local area analyses

Mineral phases and types of organic matter for (i) are summarized in Table 3 and SI 10-Table, according to the measuring area and frequency.

In summary, Fe-oxide-hydroxides (ferrihydrite, lepidocrocite, hematite) are common in all the Mn ore beds, Fe-silicates (aegirine) are common in the Mn-1 ore bed, and Fe-sulphide (pyrite) rarely occurs. Variable Mn oxides and hydroxides (todorokite, ramsdellite, pyrolusite, cryptomelane), and oxide-silicates (braunite, serandite) are the main Mn ore minerals. Besides Fe and Mn ore minerals, feldspar, chlorite, celadonite, kaolinite group-dickite, apatite, and quartz are moderate or minor mineral components. Variable types of organic matter occur in all samples.

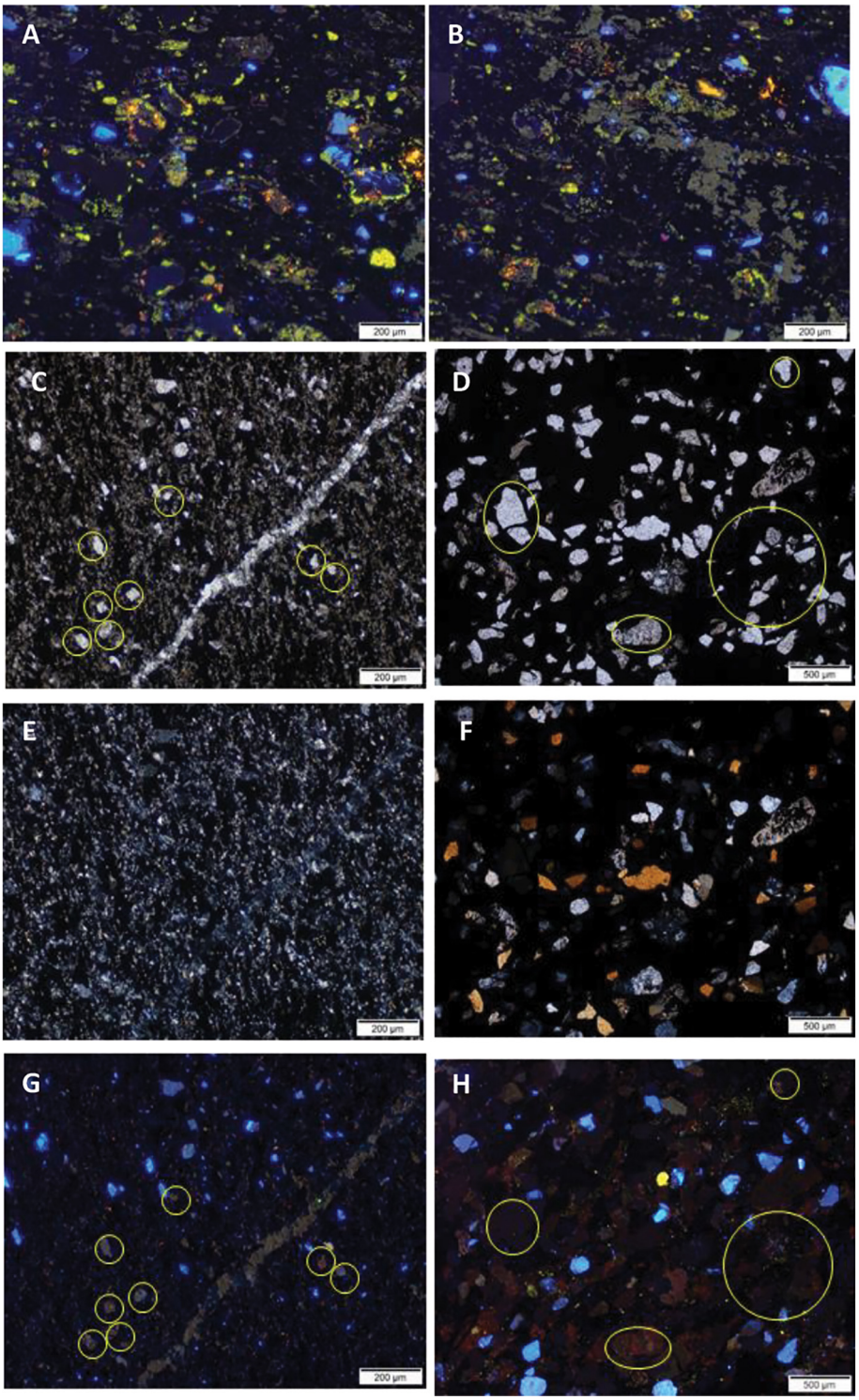

Fig. 7. Mineralogy observed under cathodoluminescence microscopy. (A, B) Typical CL image of Mn-1 samples. Bright blue luminescence is characteristic of kaolinite group-dickite (supported by Raman spectroscopy, Götze et al., 2002); bright yellow minerals are apatite grains; the fine-grained rhodochrosite (mixed carbonate) show dull reddish (orange) luminescence color. (C, E, G) transmitted light photos by 1 N, crossed N, and CL images of the same area of sample 7. (D, F, H) transmitted light photos by 1 N, crossed N, and CL images of the same area of sample 10. Circles show the clastic-like but non-luminescent mineral grains. (For interpretation of the references to color in this figure legend, the reader is referred to the web version of this article.)

5.2.2. Analyses of kremydilite

Three profile analyses in kremydilite sample 48B were made (Figs. 4K and 8). Two profiles crossed the concentric shells of the kremydilite structure on opposite sides (A and C), and one profile crossed the inner part (B).

All concentric shells and the parts intersected between these shells are heterogenous and very fine-grained. Considering that minerals represent the remnants of primary Mn and Fe minerals, each measuring point in the concentric shells and intersected parts resulted in a mixture of minerals, with often poorly crystallized phases.

All shells and the inner part are heterogeneous and very fine-grained. Each measuring point resulted in a mixture of minerals, with often poorly crystallized phases like ferrihydrite. The shells —observed visually—often have the same mineralogy (cryptomelane, hollandite, hematite, rhodocrosite, and pores). The mineralogy of the two sides of the structure are asymmetric (Fig. 8D). *Profile A* (Fig. 8B), from the margin toward the inner part, contain rhodochrosite-goethite, manjiorite-todorokite, minor ferrihydrite-cryptomelane (6 shells), and in the vicinity of the inner part, cryptomelane-ferrihydrite. *Profile C*, from the margin toward the inner part, contain braunite-rhodochrosite,

Table 3
Mineral composition.

Samples →Minerals ↓	COR-6	COR-7	COR-10	COR-31	COR-32	COR-36A1	COR-78F3
Mn minerals							
todorokite	*						
ramsdellite	*						
cryptomelane	*				*	*	*
pyrolusite					*		
romanéchite						*	
serandite	*						
braunite	*		*				
Fe minerals							
ferrihydrite	*			*	*	*	*
lepidocrocite		*					
hematite				*	*		*
aegirine	*						
pyrite				*			
Other minerals							
Apatite		*		*	*		
feldspar (albite, anortite)		*	*		*		
Chlorite	*		*				
Quartz				*	*		
Kaolinite/ dickite				*			
celadonite				*			
Organic matter	*	*	*	*	*	*	*

braunite-goethite-rhodochrosite (3 shells), braunite-cryptomelane-rhodochrosite, braunite-rhodochrosite, braunite, cryptomelane-ferrihydrite-rhodochrosite (2 shells), cryptomelane-ferrihydrite (2 shells), and cryptomelane-braunite, and in the vicinity of the inner part, cryptomelane-ferrihydrite. *Profile B*, representing the inner part from the shells to the center, contain cryptomelane-ferrihydrite, ramsdellite-rhodochrosite, birnessite-rhodochrosite (2 zones), cryptomelane-quartz-rhodochrosite, cryptomelane-birnessite-dolomite, cryptomelane-quartz-rhodochrosite, ferrihydrite-cryptomelane-dolomite-quartz, and cryptomelane-quartz-dolomite. Varying amounts of pores, with or without organic matter, are characteristic in all layers and in the central parts (Fig. 4).

In summary, mineralogical assemblages contain concentric zones (or "shells") of poorly crystallized, preserved Mn (birnessite, todorokite) and Fe minerals (ferrihydrite), and mainly more stable cryptomelane, hollandite, braunite, hematite, goethite, and rhodochrosite. *Profile C* mineral components are more stable. More stable minerals represent greater degree of crystallinity.

5.2.3. Analyses of oblate (bubble-like) structures

Based on OM of sample 36-A1, the outer and inner matrix and also the dark spots of the oblate structures appear very similar, with only the reflective color differing slightly (SI 11-Fig). FTIR analyses resulted in a similar mineralogy and variable organic matter composition, as the sample is very fine-grained and heterogeneous (Fig. 9). The peaks of most of the minerals show broad bands and low intensities, which are characteristic of disordered, poorly crystallized quartz, carbonates, and feldspar.

Out of the oblate structures, the ore contains a matrix, micro-nodules, and dark spots. The micro-nodules and the matrix consist of cryptomelane, ferrihydrite, minor goethite, rhodochrosite, and variable organic matter. The analyzed dark spot in the outer part consists of pores, cryptomelane, ferrihydrite, minor goethite, rhodochrosite, and organic matter.

There are no micro-nodules inside the oblate structure. The light part of the matrix inside the oblate structure contains cryptomelane, ferrihydrite, quartz, minor dolomite, and organic matter. The dark part comprises dolomite, ferrihydrite, cryptomelane, and organic matter. Inside, the dark spot consists of ramsdellite, quartz, minor dolomite, and organic matter (SI 11-Table).

The oblate, rim structure, separating the outer and inner parts, consists of two phases: (1) the fine-grained rim built up of ferrihydrite, minor goethite, and organic matter; and (2) the coarse-grained phase, which is a mixture of cryptomelane, disordered quartz, rhodochrosite, dolomite, traces of braunite, and variable organic matter. Comparing

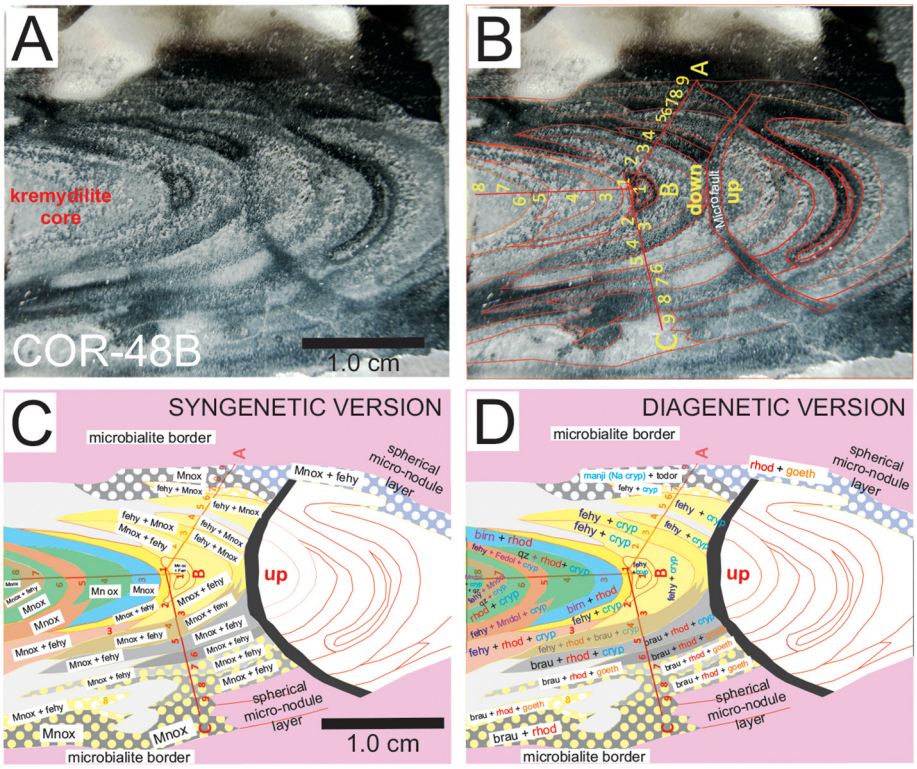

Fig. 8. Results of the FTIR analyses of the kremydilite sample 48-B and interpretation of the results. (A-B) Image of sample (A), its concentric shells (layers) and location of the analyzed points (B). (C) Simplified proposed syngenetic minerals that build up each layer. (D) Interpretation of early diagenetic minerals detected by FTIR. Abbrev.: fehy-ferrihydrite; Mnox-Mn oxide and hydroxide; manji-manjiorite; todor-todorokite; cryp-cryptomelane; birn-birnessite; qz-quartz; rhod-rhodochrosite; Mndol-Mn-bearing dolomite; brau-braunite; goeth-goethite; spherical micro-nodules border: fluffy micro-noduliferous host material. (For a colour version of this figure, the reader is referred to the web version of the article.)

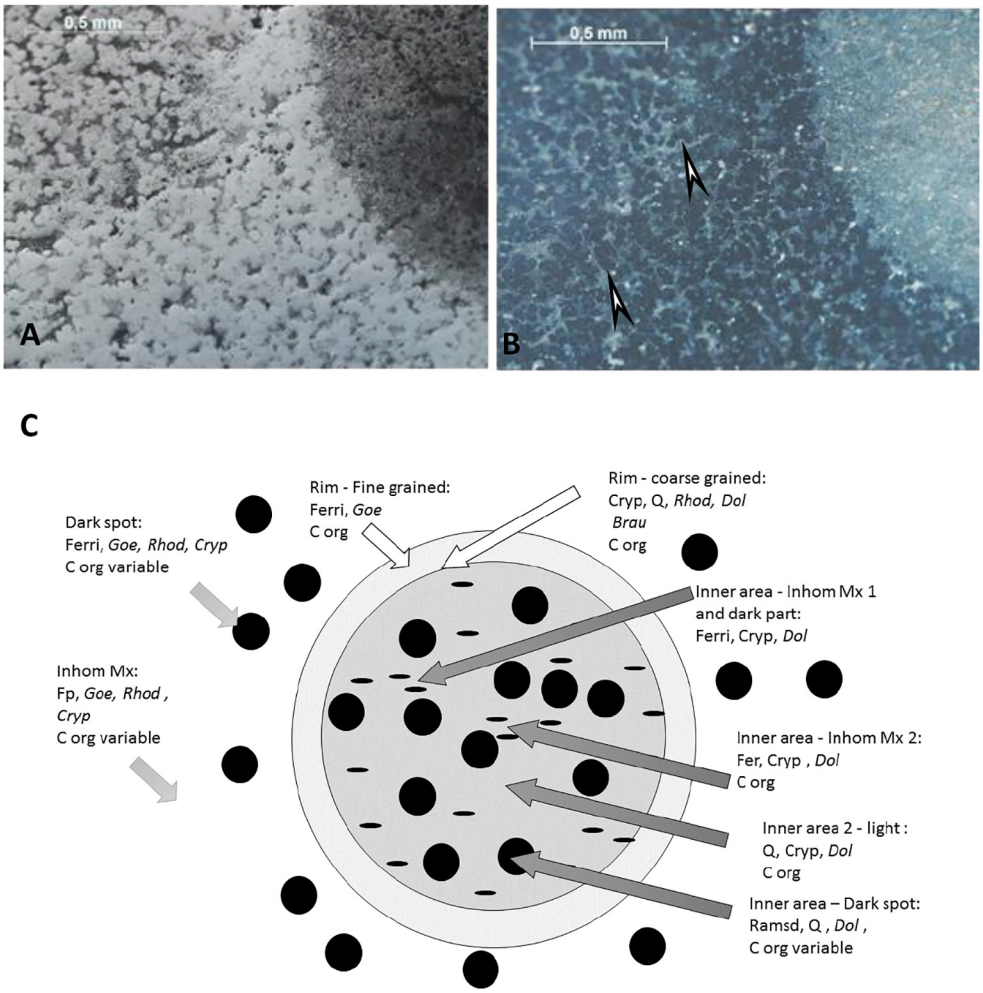

Fig. 9. Representative part of oblate structure, sample 36-A (A-B) and mineral distribution (FTIR)(C). (A-B) Microtexture of a part of oblate structure, OM, reflective mode (1 and xN), arrows show mineralized microbial signatures and diffusion channels. Abbrev: Ferri-ferrihydrite; Goe-goethite; Rhod-rhodochrosite; Cryp-cryptomelane; C org-organic matter; Q-quartz; Dol-dolomite; Brau-braunite; Ramsd-ramsdellite; Mx-matrix material; inhom-inhomogenous, italic-the component is poorly crystallized, minor.

the outer and inner parts, differences in mineralogy are reflected in the type of carbonate (rhodochrosite outside and dolomite inside), the Mn oxides of the dark spots (cryptomelane outside and ramsdellite (γ-MnO_2) inside), and the occurrence of quartz in the inner part and rim, and feldspar in the outer part. On the outside of the oblate structure, the rock contains pores and the typical (micronodule-bearing) microtexture of Mn-2 and 3, whereas inside, the micro-noduliferous textures do not exist, and pores are partially filled by hollandite.

5.3. Raman spectroscopy

Nearly 11,000 spectra were taken for micro-mineralogical and organic matter composition determinations as well as for the distribution of minerals according to the thin section profiles. Representative analyzed profiles are shown in Fig. 10 and SI 12-Fig. The mineral distribution was evaluated visually based on a series of Raman profiles at the 10-μm scale (Fig. 10, SI 12-Fig). The determined minerals, including FTIR data, are summarized in Table 4. Variable Mn oxides and hydroxides, Mn oxides-silicates, Mn carbonates, variable Fe oxides hydroxides, Fe silicates, Fe sulfide, ore minerals, apatite, feldspar (albite and orthoclase), mica (muscovite, chlorite, celadonite), kaolinite-dickite, barite, carbonates (strontianite, dolomite, ankerite), and quartz occur in the Mn ore beds. Variable organic material is also an important constituent. Based on low intensity and broad peaks, the minerals are poorly crystallized and cryptocrystalline. The representative samples contain a mixture of poorly crystallized mineral phases and organic matter.

5.3.1. Mineral distribution in profiles by Raman spectroscopy

A distribution of minerals is evident in all samples, alternating micro-laminae (a few tens of μm thick) along with the kremydilite inner part (Fig. 10, SI 12-Fig). This alternating micro-lamination refer to mineralized microbial cycles in the sediment pile. The documented distribution of minerals in the Mn ore beds is the following:

Mn-1 from Figueirinha Mine

- Sample 4B – Hematite (rarely aegirine)/rarely quartz alternation, starting with Mn (braunite) alternation and random apatite, and K-feldspar.
- Sample 7 – Aegirine/braunite cycles with randomly occurring apatite, mica, and K-feldspar.
- Sample 10 – Aegirine-hematite/quartz alternation (Fe cycles) and Mn cycles superposed (braunite, serandite, hausmannite) occur with randomly occurring apatite, barite, feldspar (albite, K-feldspar), and strontianite.

Mn-1 from São Domingos Mine

- Sample 31 – Hematite (rarely kaolinite/dickite)/quartz alternation (Fe cycles), and Mn cycles superposed (braunite, manjiorite,

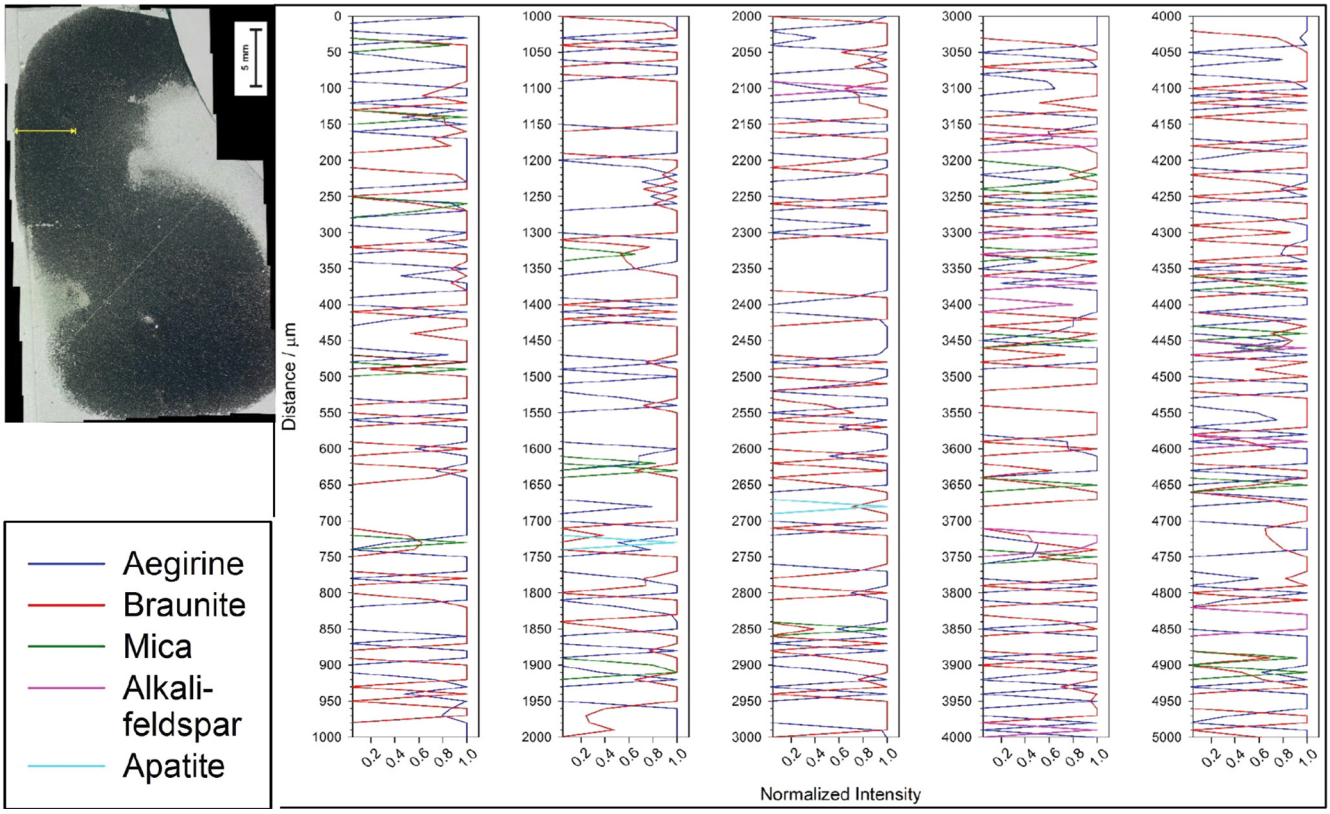

Fig. 10. Raman profiles. Representative alternating (cyclic) mineral micro-lamination in sample 7 (Mn-1) (for detailed section see SI 12-Fig). (For interpretation of the references to colour in this figure legend, the reader is referred to the web version of the article.)

jacobsite, todorokite, romanèchite).

Mn-2 from Urucum Mine

- Sample 75–2 – Only Mn minerals occur, but jacobsite and hollandite contain Fe. Jacobsite alternate with cryptomelane, ramsdellite, and hollandite. Ramsdellite is the most oxic phase. In the zone of kremydilite, the micro-lamination turns into random mineral distribution. Accessory minerals are: romanèchite (psilomelane), manganite, todorokite, pyrite, and pyrolusite.
- Sample 75-B5 – Goethite is frequent only in this sample. Representative Mn cycles are composed of cryptomelane, hollandite, and occasionally, braunite. Micro-lamination is disordered, and in those zones, random mineral distribution occurs, but locally micro-lamination is well visible. Accessory minerals are: jacobsite, manganite, ramsdellite, todorokite, hausmannite, romanèchite, pyrolusite, ferrihydrite, apatite, and mica.
- Sample 78-D1 – Hematite (Fe cycle) alternate with Mn oxide cycles (cryptomelane-hollandite) forming double microbial ore forming lamination. Cryptomelane and hollandite occur together. Hematite and braunite also occur together, but braunite occurs separately, too. Braunite binds to hematite. Locally, pyrolusite, birnessite, romanèchite, jacobsite, manganite, ramsdellite, hausmannite, serandite, ferrihydrite, goethite, mica, and apatite occur.

Mn-3 from MCR Mine

- Sample 81 – Hematite alternates with Mn oxide (cryptomelane-hollandite). Accessory minerals are: todorokite, ramsdellite, jacobsite, rancieite, pyrolusite, birnessite, braunite, ferrihydrite, magnetite, and mica.

5.3.2. Mineral phase transitions by Raman spectroscopy

Microscale mineral phase transitions offer very important information on syngenetic and diagenetic formation processes. Mineral compositions of Urucum samples also provide information on this aspect, which explains the focus on specific mineral transitions.

5.3.2.1. Aegirine. Aegirine is common in Mn-1, occurring as an alternating mineral with braunite. A detailed study on the phase transition was made for sample 4B (Fig. 11). The microtexture of aegirine resembles a vermiform network that intrudes into the quartz. The quartz occurs in the undulating hematite network as a gel-like segregated silica. Aegirine is present at the contact of quartz, and riebeckite seems to consume aegirine. This relationship shows that aegirine and riebeckite consume quartz. At the contact of segregated quartz, hollandite/vernadite and apatite occur. Braunite binds to hematite in the vicinity of quartz.

5.3.2.2. Braunite. Braunite also consumes segregated quartz similarly to aegirine, in a vermiform habit, and is in close contact with the hematite network (Fig. 12) (sample 4B). Segregated quartz also contains K-feldspar. Hematite occur as small clusters and contains an undulating network as mineralized biomats.

5.3.2.3. Cryptomelane. All the spectra taken in the micro-nodules (cell colonies) and matrix material show dominant vernadite/hollandite-type Mn-oxides-hydroxide composition and a greater or less amount of cryptomelane and variable organic matter (sample 75-2). The minerals are in a cryptocrystalline mixture with variable amounts. The textural differences do not correspond to significant mineralogical differences (Fig. 13, SI 13-Fig). The central part of the micro-nodules consists of hollandite/vernadite and organic matter, around which cryptomelane, pyrolusite and ramsdellite occur.

Table 4
Mineral assemblage in Mn ore beds and typical minerals indicative of Eh-pH ranges in Urucum based on environmental mineralogy.

Minerals/Processes	Chemical formula	Mn-1	Mn-2	Mn-3	Eh		pH			Microbiallly
Mn mineral assemblage					Ox-subox	Anox	Acidic	Neutral-slightly alkaline	Alkaline	Mediated
Oxides and hydroxide										
Pyrolusite	$Mn^{4+}O_2$	*	*	*	*					
Ramsdellite	$Mn^{4+}O_2$	*	*	*	*					
Nsutite	$(Mn^{4+}Mn^{2+})(O,OH)_2$		*		*				*	
Hausmannite	$Mn^{3+}_3O_4$	*	*							
Cryptomelane	$KMn^{4+}_6Mn^{2+}_2O_{16}$	*	*	*						
Jacobsite	$Mn^{2+}_{0.6}Fe^{2+}_{0.3}Mg_{0.1}Fe^{3+}_{1.5}Mn^{3+}_{0.5}O_4$	*	*	*						
Manganite	$Mn^{3+}OOH$	*	*							
Vernadite δMnO_2 (wad)	$(Mn^{4+}Fe^{3+}CaNa)(OOH)_2{*}nH_2O$	*	*							*
Todorokite	$Na_{0.2}Ca_{0.05}K_{0.02}Mn^{4+}_4Mn^{3+}_2O_{12}{\bullet}3(H_2O)$	*	*	*	*			*		*
Birnessite	$Na_{0.7}Ca_{0.3(}Mn^{3+}\ Mn^{4+})_7O_{14}{\cdot}2.8H_2O$	*	*	*	*			*		*
Romanèchite (psilomelane)	$[(Ba,H_2O,Mn_5O_{10},\ Ba(Mn^{4+},\ Mn^{3+})O_{10}{\cdot}1.4H_2O)]$	*	*	*						
Hollandite*	$Ba(Mn^{4+},Mn^{2+})_8O_{16}$	*	*	*						
Manjiroite	$Na(Mn^{4+}_7Mn^{3+})O_{16}$	*								
Manganite	$Mn^{3+}OOH$	*			*					*
Carbonates										
Rhodochrosite	$MnCO_3$	*						*		*
Oxides-silcates										
Serandite	$NaMn^{2+}_{1.5}Ca_{0.5}Si_3O_8(OH)$	*	*							
Braunite	$Mn^{2+}Mn^{3+}_6SiO_{12}$	*	*	*	*				*	*
Fe mineral asssemblage										
Oxides and hydroxides										
Ferrihydrite	FeOOH	*	*	*	*			*		*
Lepidocrocite	$Fe^{3+}O(OH)$	*						*		*
Hematite	Fe_2O_3	*	*	*	*					
Goethite	FeOOH	*	*		*					
Magnetite	Fe_2O_3		*	*		*				
Sulfides										
Pyrite	FeS_2	*	*			*				*
Silicates										
Aegirine	$Ca_{0.75}Na_{0.25}Mg_{0.5}Fe^{2+}_{0.25}Fe^{3+}_{0.25}(Si_2O_6)$	*			*				*	
Riebeckite	$Na_2(Fe^{2+}_3Fe^{3+}_2)Si_8O_{22}(OH)_2$	*								
Celadonite	$KMg_{0.8}Fe^{2+}_{0.2}Fe^{3+}_{0.9}Al_{0.1}Si_4O_{10}(OH)_2$	*			*			*		*
Chlorite	$Mg_{3.75}Fe^{2+}_{1.25}Si_3Al_2O_{10}(OH)_8$	*								
Chamosite	$(Fe^{2+}Mg)_5Al(AlSi_3O_{10})(OH)_8$	*				*				
Others										
Oxides - hyydroxides										
Quartz	SiO_2	*					*			*
Carbonates										
Dolomite	$CaMg(CO_3)_2$	*			*			*		*
Strontianite	$Sr(CO_3)$	*			*			*		
Ankerite	$Ca(Fe^{2+},Mg)(CO_3)_2$	*								
Silicates										
Orthoclase	$KAlSi_3O_8$	*						*		
Albite	$NaAlSi_3O_8$	*						*		
Kaolinite/dickite	$Al_2Si_2O_5(OH)_4$	*			?	?	*			
Muscovite	$KAl_3Si_3O_{10}(OH)_{1.8}F_{0.2}$	*	*	*						
Silicate-carbonate-sulphate										
Cancrinite	$(NaCa\ldots)(Al_6Si_6O_{24})(CO_3,SO_4)_2{*}2H_2O$	*								
Phosphates										
Apatite	$[(Ca_{10}(PO_4)_6(OH,\ F,\ Cl)_2]$	*	*		*			*	*	*
Sulphates										
Barite	$Ba(SO_4)$	*			*			*		
Gypsum (anhidrite)	$CaSO_4{\cdot}2H_2O$		*							
Johannite	$Cu(UO_2)_2(SO_4)_2(OH)_2\ 8H_2O$	*	*							
Organic material		*	*	*						

Mineral assemblage is based on Raman and FTIR spectroscopy analyses.
Eh-pH ranges and microbially mediated mineralogy is based on: Listova (1961); Harder (1976, 1978); Trudinger and Swaine (1979); Berner (1980); Giovanoli (1980); Sung & Morgan (1981); Cole & Shaw (1983); Ewers (1983); Maynard (1983); Coleman (1985); Skinner (1993); Ehrenreich & Widdel (1994); Wignall (1994); Mandernack et al. (1995); Straub et al. (1996); Banfield & Nealson (1997); Konhauser (1998); Herdianita et al. (2000); Ehrlich (2002); Bazylinski & Frankel (2003); Villalobos et al.(2003); Bargar et al. (2005); Dupraz & Visscher (2005); Morgan (2005); Bodeï et al. (2007); Schwertmann & Cornell (2007); Dupraz et al. (2009); Chan et al. (2011); Polgári et al. (2012a,2012b,2013,2016a,2016b); Biagioni et al. (2014); Johnson et al. (2016); Gyollai et al. (2017); Mloszewska et al. (2018).
* Hollandite *(empirical)* $Ba_{0.8}Pb_{0.2}Na_{0.1}Mn^{4+}_{6.1}Fe^{3+}_{1.3}Mn^{2+}_{0.5}Al_{0.2}Si_{0.1}O_{16}$.

5.3.3. Oblate structures

Detailed Raman measurements were elaborated on a representative oblate structure, used to compare the mineral composition and distribution inside the oblate structure, in its vicinity, and in the rim (sample 36-A1, Fig. 14, SI 14-Fig).

The dark spots in the outer matrix are mainly pores, except dark

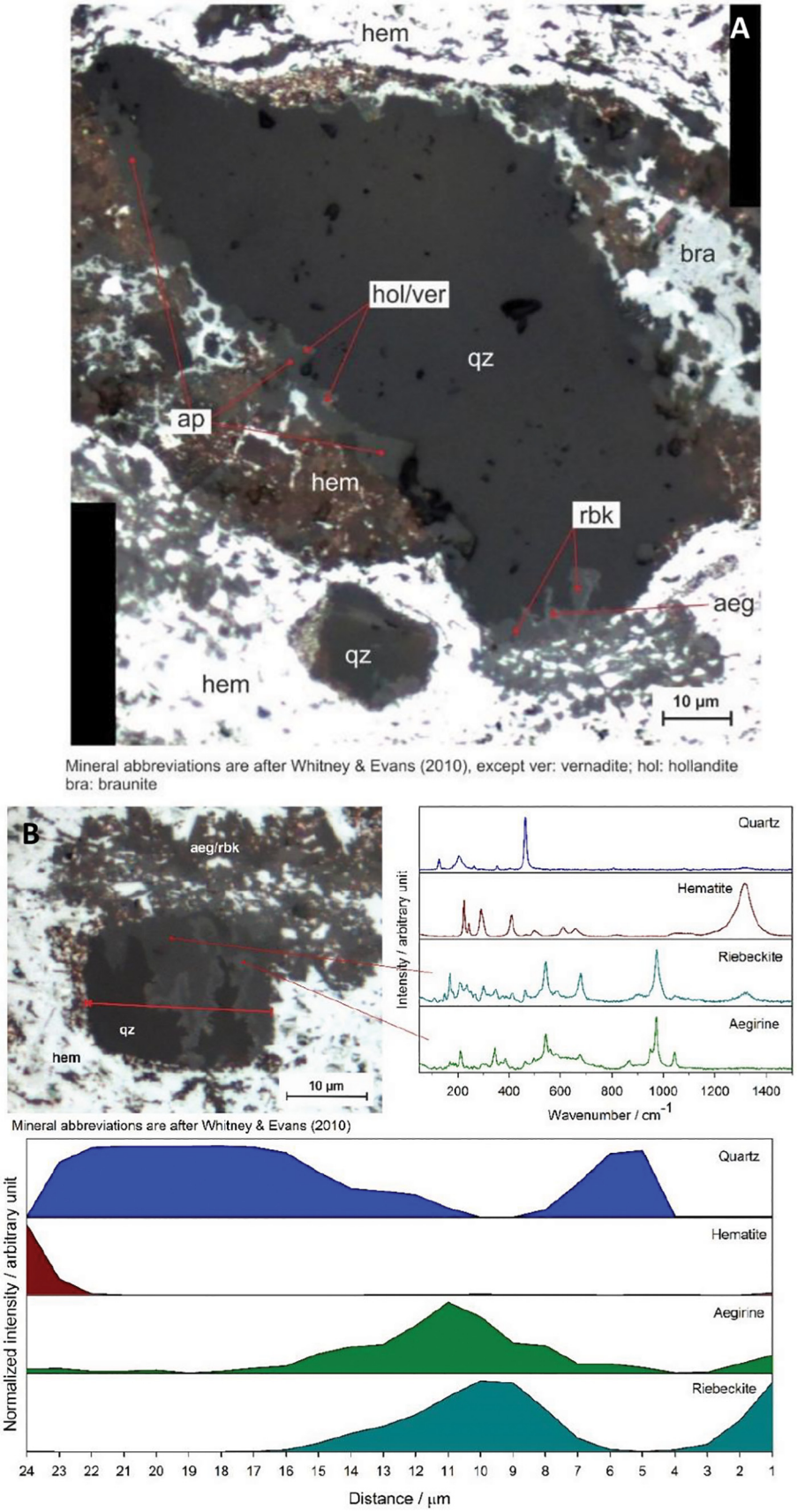

Fig. 11. Distribution of minerals in sample 4B (A-B) by Raman spectroscopy. Aegirine, riebeckite, braunite, quartz, hematite, apatite, hollandite/vernadite identified by Raman (A-B). Mineral abbreviations are after Whitney and Evans (2010) except bra = braunite, ver = vernadite, hol = hollandite. (For interpretation of the references to colour in this figure legend, the reader is referred to the web version of the article.)

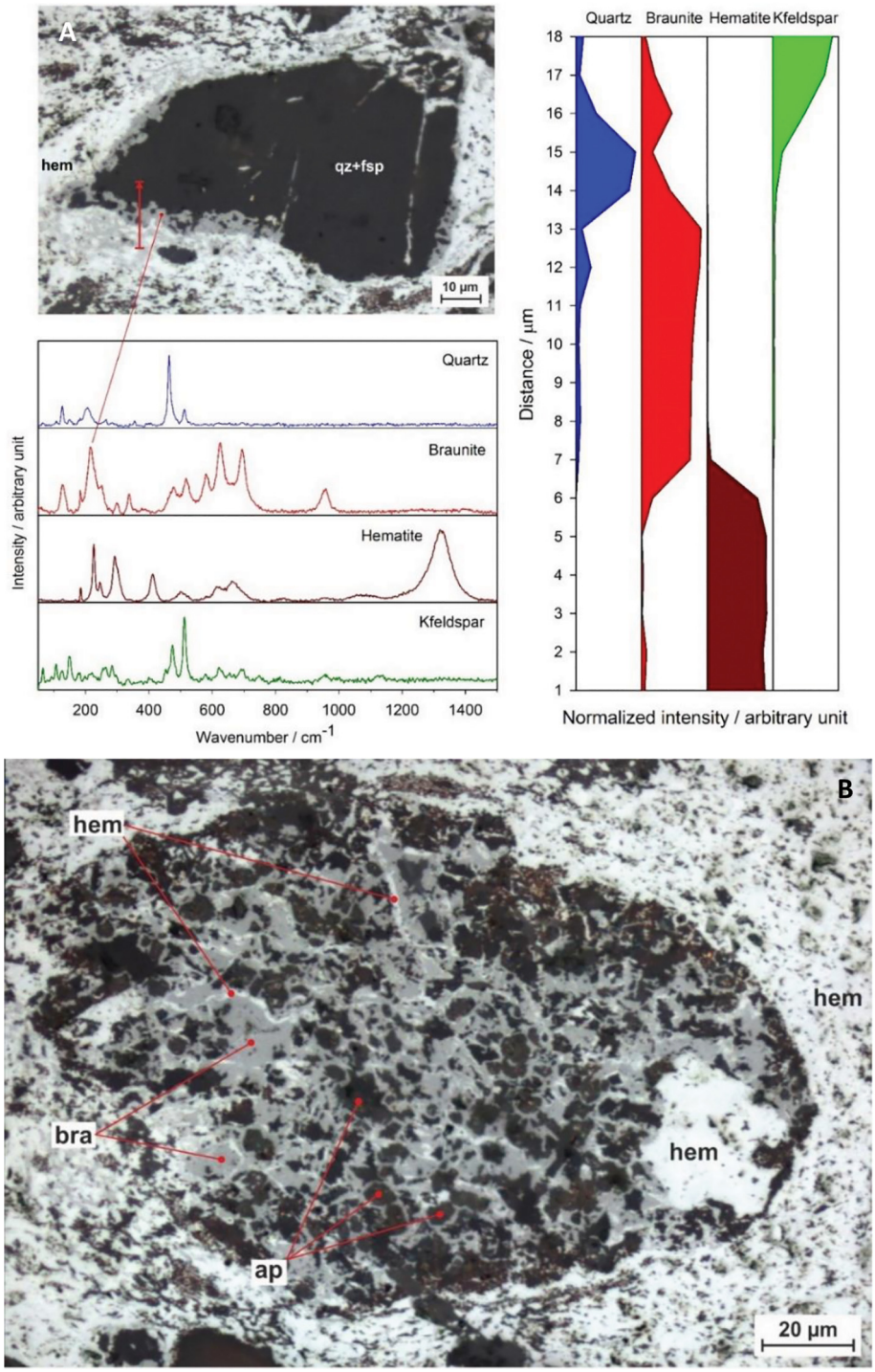

Fig. 12. Distribution of minerals in sample 4B (A-B) by Raman spectroscopy. Braunite, hematite, apatite, quartz, and K-feldspar were identified by Raman (A-B). Mineral abbreviations are after Whitney and Evans (2010); except bra = braunite. (For interpretation of the references to colour in this figure legend, the reader is referred to the web version of the article.)

porous inner rims with variable thicknesses, which are composed of a hollandite-type Mn oxide phase (dominant phase), cryptomelane, and goethite. The matrix among the dark spots is built up by hollandite, cryptomelane, and goethite.

The non-porous rim of the oblate structure mainly consists of hollandite and cryptomelane in variable amounts. Rarely fine-grained clusters of goethite occur among the hollandite-cryptomelane flakes.

In comparing the mineral phases and distribution in the outer, inner, and rim areas of the measured oblate structure, we find that they are similar. The matrix of the inner part of the oblate structure is composed of very fine-grained goethite (ferrihydrite) and small particles of Mn oxides (hollandite and cryptomelane in variable amounts); however, hollandite is dominant in the dark spots. The mineral composition of the matrix and dark spots show a unified distribution, as any difference or significant trend in the matrix or in the dark spots was not detected.

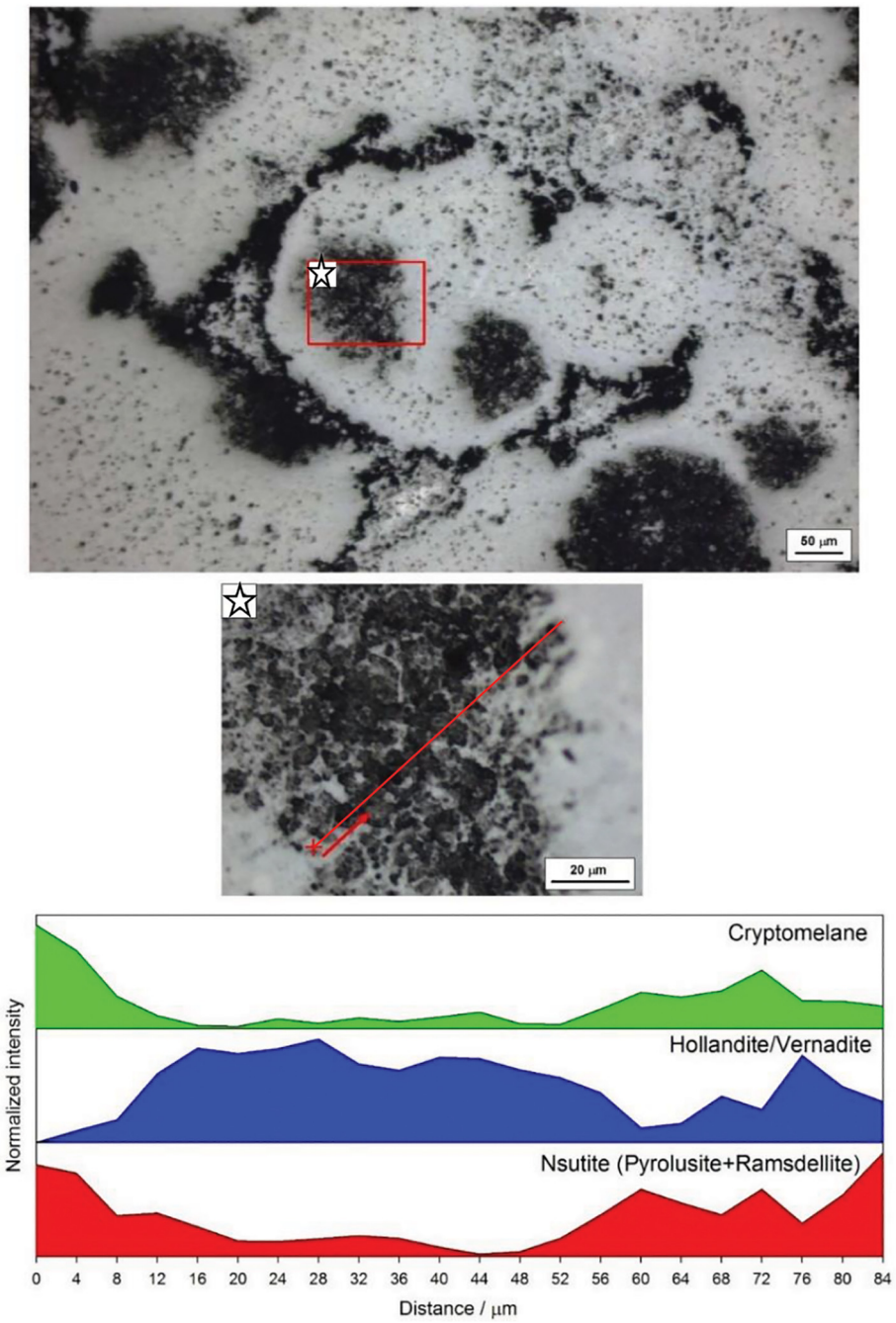

Fig. 13. Distribution of minerals in sample 75–2 by Raman spectroscopy. Cryptomelane, hollandite/vernadite and nsutite (pyrolusite + ramsdellite) were identified in a micronodule, as shown in Fig. 5C-D. (For interpretation of the references to colour in this figure legend, the reader is referred to the web version of the article.)

5.3.4. Organic matter

The organic matter of Mn-1 ores from Figueirinha (samples 4B, 7, and 10) and São Domingos (sample 31) area are dominated by two bands near 1320 and 1610 cm^{-1}, which are D and G bands of hydrogenated amorphous carbon (Chen et al., 2007). This ore bed contains also traces of aromatic hydrocarbons (825 cm^{-1}), and skeletal stretching of C=C and C=O molecules. Bands of aliphatic hydrocarbons occur at 1000–1280 cm^{-1} (Okolo et al., 2015) (samples 4B, 7, 10, 31), 1300–1390 cm^{-1} represents CH_3 (Jehlička et al., 2009), and 1487 cm^{-1} refer to CH_2/CH_3 vibrational mode (Jehlička et al., 2009) (samples 7, 10). The band at 1518 cm^{-1} refers to the C=C stretching in polyenes (sample 31), while 1620–1820 cm^{-1} show the C=O vibration of oils (Orange et al., 1996) (sample 4B).

The organic matter of ores of Mn-2 (Urucum West Mines) (samples 75–2, 78-D1, and 75-B5), contain bands of aliphatic hydrocarbons (1104 cm^{-1}), CH_3, and the D and G band of hydrogenated amorphous carbon based on bands near 1320 and 1610 cm^{-1}. The sample 75–2 contains only the D and G band of amorphous hydrocarbon, whereas sample 75-B5 contains the aromatic hydrocarbon (825 cm^{-1}) bands of CH_2/CH_3 vibration (1386, 1469 cm^{-1}), and C=O vibration of oils (1750–1800 cm^{-1}). The sample 78-D1 has bands D and G of hydrogenated amorphous carbon and traces of CH_2/CH_3 vibrational mode of aliphatic hydrocarbon (1345, 1362 cm^{-1}). The sample of the Mn-3 ore bed (MCR Mine, sample 81) contains mostly hydrogenated amorphous carbon (D and G bands at 1317 and 1600 cm^{-1}) and traces of aliphatic (1000–1200 cm^{-1}, 1469 cm^{-1}) and aromatic hydrocarbons (825 cm^{-1}). Only 60 of 1903 spectra contains organic material.

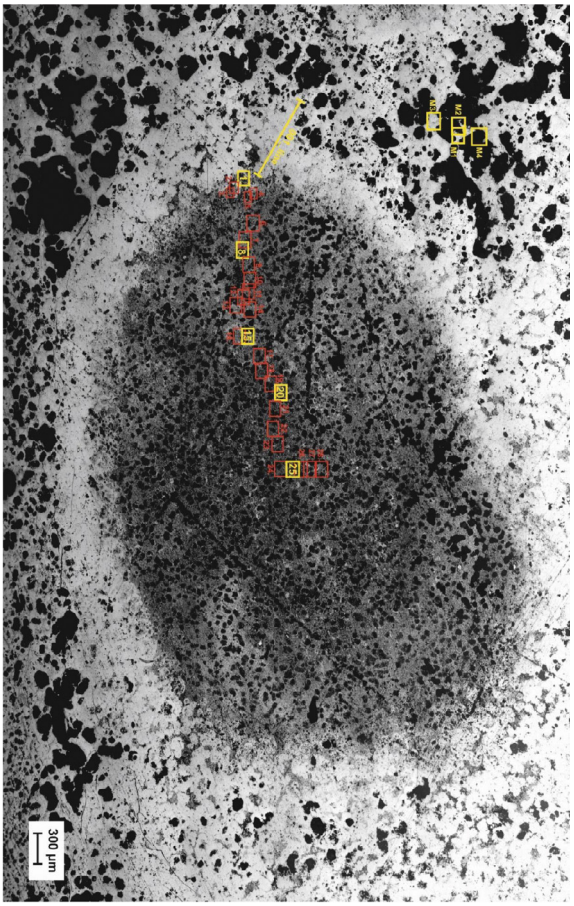

Fig. 14. Composite map from the investigated oblate structure sample 36-A by Raman spectroscopy—measured areas are indicated on the picture (those places which are detailed in SI 14-Fig are in yellow color). Abbrev.: M-matrix area, 001 line-rim area. (For interpretation of the references to color in this figure legend, the reader is referred to the web version of this article.)

6. Discussion

6.1. Sedimentation age and environments

The presence of long chain oil type in manganese layers with kremydilite indicates that temperatures were hardly larger than 90 °C, which eliminates the possibility that the Jacadigo Group' rocks have been metamorphosed. This find makes it likely that the $^{40}Ar/^{39}Ar$ age of the Mn-1 layer is effectively 547 ± 3 to 513 ± 4 Ma, the ages of braunite and muscovite determined by Piacentini et al. (2013). This age seems to be reinforced by that determined by Babinsky et al. (2008), which dated detrital zircons (U–Pb SHRIMP) from a volcanic ash layer intercalated with carbonate rocks of the Tamengo Formation at 543 ± 3 Ma.

Corumbella and stromatolite occurrences and field information published by Biondi and Lopez (2017) indicate that the Santa Cruz Formation (BIFs) and the manganese layers sedimented at the same time or after the Bocaina Formation; and that the ages of these rocks are about 550 Ma. The age of this fossil in the ironstones of the Santa Cruz Formations (Jacadigo Group) and limestones of the Tamengo Formation (Corumbá Group) was estimated at ca. 550 Ma (Germs, 1972; Grant, 1990; Grotzinzer et al., 1990; Hofmann and Mountjoy, 2001; Bengtson, 2002). Also, the proposed age of this horizon was 555–542 Ma by ichnofossils, identified by Parry et al. (2017), in the Bocaina Formation.

There is no diagnostic evidence that sedimentation occurred during some glacial period or during some glaciation, as initially proposed by Urban et al. (1992). The only arguments of these authors were: (a) the presence of the granite blocks they interpreted as dropstones, without even observing whether any of these blocks have faceted, friction-sectioned sides, and/or have striated faces, as is typical of dropstones. These characteristics were never observed in the Urucum (Trompette et al., 1998; Freitas et al., 2011; Biondi and Lopez, 2017). (b) To consider the Santa Cruz Formation, with at least 400 m thick BIFs, as similar to the Rapitan Formation, with less than 10 m thick BIFs (Young, 1976). As the Rapitan Formation would be Ediacaran and of glacial origin (Young, 1976), Urban et al. (1992) inferred that the Santa Cruz would have the same origin; and most subsequent authors adopted this idea. However, keeping in mind that this hypothesis is traditionally defended by many authors (e.g. Angerer et al., 2016), it should be discussed.

The last glacier related to snowball earth, and the sedimentation of Rapitan-denominated BIFs, was the Marinoan glaciation, which began at about 650 Ma and ended at about 635 Ma. Considering all the information presented above, the Urucum's BIFs, ironstones and manganese layers sedimented about 550 Ma ago, 85 Ma after the end of the Marinoan and the snowball glaciations. The Gaskiers glaciation, which existed for 340,000 years (579.9–579.6 Ma), has occurred about 29 Ma before — the Jacadigo Group sedimentation, and could hardly influence its sedimentation. It remains, therefore, to relate the formation of the Jacadigo Group with Baykonurian glaciation (547–545.5 Ma), so far recognized only in Asia and Africa (Chumakov, 2009; and Chumakov, 2011; Germs and Gaucher, 2012). We therefore propose to consider the possibility that the sedimentation of the BIFs and manganese layers of the Santa Cruz Formation occurred during the Baykonurian glaciation, which would explain the existence of what is interpreted by Urban et al. (1992), among other authors, as dropstones.

We hold the view that Mn-1 was most likely formed during the first inundation of the ancient graben by the fluvial, oxidative sediments that gave rise to the Urucum Formation. Unit Mn-1 contains predominantly siltic and sandy, ferruginous clastic rocks, cemented by microbially mediated Fe minerals (e.g., aegirine), and Mn-oxide and silicate (braunite, serandite, and hollandite). The areas of Figueirinha and São Domingos mines have a larger concentration of manganese in Mn-1, which are contained in clast-bearing massive ores. The upper Mn-1 layers in the Figueirinha and São Domingos mines, which include amygdalites, were probably deposited in the basin depocenter, where the amygdalites formed from hydrodynamic flux. Layers Mn-2 and Mn-3 formed in "offshore" (= greater depth) environments during periods of tectonic quiescence, when fine, clastic quartz fragments and other detrital sedimentation ceased.

6.2. Mineralogical interpretations

Microtextural evidence in all the studied samples appears as dense features, and the mineral types and embedded variable organic matter raise the microbially-mediated formation of the ore beds, which we argue occur as microbialites (MMPT). Two microbial ore forming systems are proposed as dual systems, characterized by Fe- and Mn-oxidizing metabolic processes (Fe-oxidizing bacteria (FeOB) and Mn-oxidizing bacteria (MnOB)).

Several studies on the genesis and preservation of oil and natural gas have shown that long chain hydrocarbons are decomposed at temperatures above 90 °C (Chilingar et al., 2005, p.138–142). Preservation in Mn-2 and Mn-3 of aromatic and aliphatic hydrocarbons, C=C stretching in polyenes, C=O vibration of oils, among others, indicates that temperatures during diagenesis were low (< 90 °C) and that syngenetic as well as diagenetic minerals were preserved, as identified by the Raman and FTIR analyses. Along with hydrocarbons, these analyses identified minerals such as birnessite and ferrhydrite, which we consider remnants of the original sedimentation, (i.e. they were not entirely destroyed during diagenesis). Remnants of syngenetic and diagenetic minerals interpreted as complex systems give a plausible

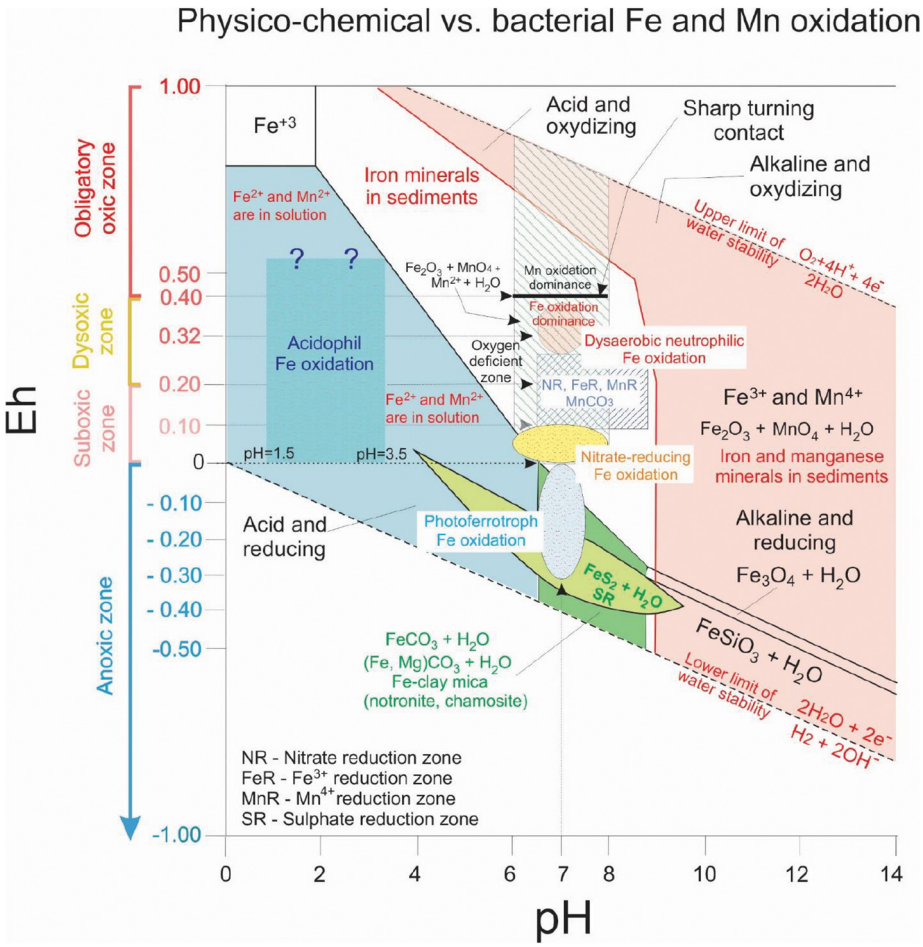

Fig. 15. Physico-chemical vs bacterial Fe and Mn oxidation (modified after Garrels and MacKenzie, 1971; Maynard, 1983). Eh in Volt. Concerning NR, FeR, MnR, and SR see Table 5 and note that "suboxic" zone is used for these diagenetic zones in the sense of an oxidant agent. Sharp-turning contact between Fe and Mn mineralization as transformation to obligatory oxic conditions is estimated at Eh = 0.4 V (DO > 2 mL/L). (For interpretation of the references to colour in this figure legend, the reader is referred to the web version of the article.)

series of processes and environmental formation conditions during sedimentation and diagenesis (Table 4, Fig. 15, SI 15-Table). The frequency of the minerals is different: the main minerals, such as cryptomelane, hollandite, hematite, and braunite, form the ore beds, but the moderate and minor minerals have also genetic importance. The Mn layers are the result of complex diagenetic processes and formation of diagenetic minerals, which include the components of the decomposition of cells and extracellular polymeric substance material (Fe and Mn bacteria, cyanobacteria, and other types; see Ewers, 1983; Wignall, 1994; Konhauser, 1998; Villalobos et al., 2003; Dupraz and Visscher, 2005; Dupraz et al., 2009; Chan et al., 2011; Gyollai et al., 2017).

Some syngenetic poorly crystallized minerals were preserved, and that serves as a starting point. For a clear understanding, a short review on the most important mineral assemblages and primary minerals is needed. Many types of minerals occur, and these can be grouped as follows.

6.2.1. Remnants of syngenetic minerals – Syngenetic Fe- and Mn-rich biomat formation

Remnant syngenetic minerals are reported as microbially mediated minerals forming under obligatory oxic (Mn) and suboxic (Fe) conditions, with neutral and semi-neutral pH. The microbially mediated Mn and Fe oxidation have different oxygen demand, and the diagenetic zones represent different oxygen conditions. The nomination "suboxic" has a double meaning which can cause discrepancies. To avoid misunderstanding, definitions are listed in Table 5. In general, Eh > 0 represent oxic conditions, but the concentration of oxygen can be different, as shown in Table 5 and Fig. 15, and the microbially mediated processes occur at a given oxygen content. Diagenetic zonation also separates the oxic, suboxic, and anoxic zones, and the oxidizing agent is O_2 in the oxic zone, NO_3^-, MnO_2, and Fe_2O_3 in the suboxic zone, and SO_4^{2-} in the anoxic zone (Berner, 1980; Coleman, 1985; Wignall, 1994; Polgári et al., 2012a,2012b).

Ferrihydrite and lepidocrocite on the Fe side, and vernadite, todorokite, birnessite, and manganite on the Mn side, are regarded as syngenetic minerals (Ehrlich, 2002). Accordingly, it is obvious that ore formation started with microbial Fe oxidation. That is why interpretation starts with a description of the Fe system.

Table 5
Environmental oxygen levels.

Environmental oxygen levels	Eh (V)	Dissolved oxygen (DO)	FeOB demand*	MnOB demand
Obligatory oxic	0.4 < Eh < 1.0	DO > 2 mL/L		x
Dysoxic	0.2–0.4	DO 0.2–2.0 mL/L	≈ 0.3	
Suboxic	0–0.2	DO 0–0.2 mL/L		
Anoxic	< 0			

* : FeOB demand is around the dysoxic-suboxic zone, and suboxic is the generally used as simplified form; abbrev: FeOB-Fe oxidizing bacteria; MnOB-Mn oxidizing bacteria (Berner, 1980; Coleman, 1985; Wignall, 1994).

6.2.1.1. Syngenetic Fe system. Understanding the biochemistry of the biomat formation is a key factor in determining the type of Fe-rich biomat that may have been involved in the formation of the Urucum Mn layers, and to define the environmental conditions. There are various types of microbial metabolisms that can oxidize Fe^{2+} in nature, which occur under varying states of oxygen-deficient conditions. Three types of Fe-rich biomats are considered for the Urucum; all are neutrophilic and consistent with basin conditions (Fig. 15): (1) Microbial neutrophilic, micro-aerobic Fe(II) oxidizing bacteria (pH ~ 8; Eh + 0.3 V) (Hallbeck and Pedersen, 1990; Ehrenreich and Widdel, 1994; Konhauser, 1998; Ehrlich, 2002) supported by mineral assemblage (ferrihydrite, goethite, hematite, celadonite); (2) Nitrate-reducing Fe(II) oxidizers in suboxic/anaerobic conditions (lack of filaments; Straub et al., 1996); and (3) Photoferrotroph metabolism in anoxic/anaerobic light-demanding conditions, which is not plausible based on mineral assemblage, which support suboxic-oxic conditions. The fourth (4) type, strongly acidic, oxic metabolism is also not plausible in the Urucum basin, and does not fit with the mineral assemblage. However, a further process we have to consider, is the non–Fe-oxidizing microbes later overgrown by Fe oxides via microbial processes (Konhauser, 1998). This cannot be excluded, but the homogenous Fe-precipitation on filamentous forms do not support this scenario as a principal process.

The rhythmic developmental stages via microbial mediation is basic. Free-living Fe(II) oxidizing bacteria exist in the lag and log phases (Novick, 1955; Zwietering et al., 1990), and stalk formation (Fe-rich biomat–mineralization) occurs during the stationary (abbrev.: stat) phase under optimal conditions (pH > 6, aerobic, cell number > 6×10^5 mL^{-1}, low organic C content, 1–3 week whole microbial population growth period; e.g., *Gallionella*-like freshwater types and *Mariprofundus*-like marine types) (Hallbeck and Pedersen, 1990; Chan et al., 2011; Polgári et al., 2012a).

Organic biomarkers were not directly associated with Fe-rich biomat structures. Raman and FTIR data show organic matter in the biomat lacework but is not diagnostic as to its type. Based on these data, the diagenesis developed more in rocks represented by sample 75-2, where only amorphous carbon remained in traces, and other type of organic material was consumed. Preservation of organic material was best in sample 75-B5, in which organic material occurs in 180 of 2447 spectra, and more complex organic material, like oils and aromatic hydrocarbons, were detected. Sample 78-D1 (SI 3-Fig) is more altered, because only traces of complex organic material were preserved, and organic material—mostly D and G bands—occur in only 60 of 3456 spectra. Biomarkers cannot be isolated because of multiphase microbial activity and extensive diagenetic overprinting.

6.2.1.2. Syngenetic Mn system. Mn-oxide formation in Mn-1 ore bed can be explained by the oxide surface catalysis model advocated by Morgan (2005). Metal-oxide surfaces are able to accelerate Mn(II) oxidation by redox reactions (e.g., hematite, goethite, lepidocrocite, and manganese dioxide; Wilson, 1980; Sung and Morgan, 1981; Davies and Morgan, 1989). Raman spectroscopy detected vernadite as poorly crystallized mineral phase in the vicinity of hematite biomat lacework (Fig. 11).

In the case of Mn-2 and Mn-3, during the development of the Mn-oxide proto-ore, the first product of microbial enzymatic Mn(II) oxidation probably was a bio-oxide (e.g., vernadite, todorokite, birnessite), similar to the experimental studies of Villalobos et al. (2003); Bargar et al. (2005); and Bodeï et al. (2007). This enzymatic Mn oxidation can be referred to as Cycle I. The demand of microbial (enzymatic) Mn(II) oxidation is obligatory oxic conditions (> 2 mL/L dissolved oxygen). This bio-oxide is an X-ray amorphous oxide similar to δ-MnO_2 (vernadite, todorokite, birnessite; all detected by Raman), which is thought to be a disordered thermodynamically unstable 7-Å-vernadite (hexagonal phyllomanganate) containing Mn(IV) vacancy defects, with very small particle sizes (< 20 nm lateral dimensions), and having only two or three MnO_2 layers stacked along the c-axis (Villalobos et al., 2003). A decrease in the dissolved Mn(II) appears to act as a reductant for the biogenic oxide and control the stability of secondary abiotic reaction products (Mn^{2+} components in minerals of Urucum support this process). Cation binding, like Mg, supports phyllomanganate transformation to stable tectomanganate (Bodeï et al., 2007). Experimental studies showed that extracellular polymers from bacteria catalyze the adsorption of Mg on the surface of the cells (Mandernack et al., 1995). Thus, the bacterial cells not only directly oxidize Mn(II) to Mn(IV), but also, in the early stages of oxidation, influence the cation composition of the Mn-oxide mineral being produced. Mineralogical changes similar to these are likely to be commonplace in natural settings where bacterial oxidation of Mn(II) occurs and may liberate sorbed metal ions or alter the rates of Mn-oxide surface processes, such as the degradation of organic molecules. It is noteworthy that microbes may exploit such mineral transformation reactions to indirectly control chemical conditions in the vicinity of the cell (Mandernack et al., 1995).

A series of detailed mineralogy and micro-textures are shown in Fig. 13 (sample 75-2 from Mn-2 ore bed). The studied part is representative for syngenetic microbial Mn oxidation. The distribution of vernadite/hollandite and very early diagenetic cryptomelane and nsutite show micro-nodules with mineralized microbial colonies with embedded organic matter, which appear to support this scenario. Recent results also comport with the study of Piacentini et al. (2013) who, based on petrographic evidence, reported that cryptomelane may not be the primary Mn mineral precipitated in the Neoproterozoic ocean floor.

6.2.2. Diagenetic minerals

6.2.2.1. Diagenetic Fe system. According to the diagenesis of Fe-rich biomats, the microbes produce poorly ordered ferrihydrite (lepidocrocite) as a primary mineral, which transforms to more ordered minerals, such as goethite or hematite (reduced form as magnetite), within a few months or years via dissolution-dehydration processes, as mentioned before (Konhauser, 1998; Schwertmann and Cornell, 2007; Gyollai et al., 2015). The main Fe oxide mineral in the filaments of our samples is hematite, but Raman analyses indicate that goethite also occurs (sample 75-B5, SI 12-Fig). In Mn-1, aegirine, and in Mn-2, rare jacobsite can represent mineralized Fe-biomats. In other rare occurrences, pyrite also occurs reflecting that locally anoxic conditions existed but did not become dominant. The fossilized Fe-rich biomats were rapidly and extensively encrusted by minerals, such as dolomite and silica, similar to what has been reported by Baele et al. (2008). Amorphous silica segregation is derived by either the destruction of organic complexes or the transformation of ferrihydrite (Baele et al., 2008).

Aegirine, occurring in cyclic microlaminae alternating with braunite in Mn-1, is the diagenetic mineral form of FeOB (Fig. 10). Aegirine forms via early diagenesis from the syngenetic Fe-oxi-hydroxides (ferrihydrite) and segregated silica, and represents a more stable mineral phase. Aegirine micro-laminae represent the Fe-oxidizing microbial cycles, and braunite represents the Mn cycle in silicified and stable form, also reported by Johnson et al. (2016). This aegirine-braunite microbialite represents oxic/suboxic conditions (Listova, 1961). High-resolution Raman investigations show that aegirine consumes segregated silica from hematitic biomat toward the segregated silica via the transitional mineral riebeckite (Fig. 11). Riebeckite is also a common constituent in BIF with aegirine reported by Savko (2006), who proposed metamorphic formation, which does not fit with our observations. In Mn-1, aegirine forms a woven network (Fig. 11), the hematitic proforma of biomat with the segregated silica. At the contact between hematite and silica, apatite, vernadite/hollandite, and braunite occur. Similar to aegirine, braunite also consumes the segregated silica. Our results fail to fit with the hydrothermal origin of aegirine proposed for Paleoproterozoic Hotazel iron-formation, South Africa (Tsikos and Moore, 2005); the cyclic occurrence, worm-like consuming behavior, and also the mineral assemblage contradicts with that scenario.

Comparison with other natural aegirine occurrences, however, such as authigenic aegirine in the lacustrine Green River Formation of Wyoming, U.S.A. (Fortey and Michie, 1978), shows a close similarity. In short, the reported authigenic formation of aegirine fits well with our results, but the source of Na instead of volcanic activity was more probably the decomposition of cell and extracellular polymeric substance organic material.

As the depth of the basin is not known, fragments of slightly lithified and re-sedimented and cemented biomats occur, a shallow marine condition cannot be excluded. In such environments, evaporitic alkaline sodium-rich conditions cannot be ruled out and indeed, are preferred for aegirine formation. The high silica concentration favors aegirine formation instead of clay minerals (Decarreau et al., 2004,2008), which only sporadically occur in the samples studied here (celadonite, chamosite).

Celadonite, a dominant mineral phase in the Mesozoic Úrkút Mn-deposit (Polgári et al. 2012b; Polgári et al., 2016a,2016b), is an Fe-mica reflecting suboxic neutral conditions. It is rare in Urucum presumably because of high silica content.

Chamosite formation is favored by seawater solutions at low temperatures with a relatively reduced pH, a low amount of SiO_2, high content of Fe^{2+} and Fe^{3+}, and a relatively high amount of Al and Mg. Aluminum may be donated to the system by organic matter as reported by Maliva et al. (1999) who showed that the aluminum content is greatly increased by complexation with organic acids. Low silica concentration in solution is the most important condition for low-temperature synthesis of clay minerals, as high silica concentration in solution inhibits their formation (Harder, 1976).

6.2.2.2. Diagenetic Mn system. In diagenesis, the stabilization of the syngenetic Mn oxide hydroxides proceeded and pure forms, such as pyrolusite, ramsdellite, nsutite, hausmannite, manganite, and variable-cation-bound forms (e.g., Na, K, Ca, Mg, Ba, Fe) such as cryptomelane, jacobsite, romanèchite, and manjiorite grew (Giovanoli, 1980; Mandernack et al. 1995; Villalobos et al. 2003; Bargar et al. 2005; Bodeï et al. 2007; Johnson et al. 2016). Of note, as described by Polgári et al. (2012b), Maynard (2014), and Johnson et al. (2016), rhodochrosite can result from the sporadic activity of heterotrophic microbes during the early stages of diagenesis. Rhodochrosite is, however, only frequent in the only fully analyzed kremydilite sample shown in Fig. 8. Otherwise, these poorly mineralized cryptocrystalline mineral phases mix in a variable amount in the microlaminae as a manifestation of mineralized Mn cycles. Similarly, pyrolusite, ramsdellite, and romanèchite indicate Mn precipitation via diagenesis from low-temperature pore fluids as reported by Rajabzadeh et al. (2017).

6.3. Combined diagenesis of the two ore-forming microbial systems and other microbial forms

Harder (1978) noted that "…the silica content of sedimentary iron ores is found in quartz and different iron-containing clay minerals. Chamosite, greenalite, cronstedtite, nontronite, glauconite, and thuringite are common minerals in sedimentary iron ores. In general, all these minerals are extremely fine-grained." We find that the formation of Mn-1 manganese ore in Urucum influenced and changed this general protocol, despite the observation of quartz, local Fe mica, and Fe clay. Highly alkaline pore water conditions in diagenesis (accompanied by elevated Na content) caused aegirine precipitation instead of smectite (Decarreau et al. 2004,2008). Low silica content and Si/Fe ratio lead to chamosite formation under reduced pH and Eh conditions. The high silica content probably influenced silica uptake of variable Mn oxide-hydroxide minerals. Through stabilization caused by diagenetic processes, the Mn oxide hydroxide bound not only Fe^{2+} and Fe^{3+} (e.g., jacobsite, hollandite minerals), but also silica (braunite, serandite), to form a highly variable content of oxide-silicate mixed minerals. These are characterized by highly variable composition. Texturally, mineral habits are strongly modulated (and perhaps templated) by extracellular polymeric substances that form a network of pore spaces.

Braunite alternates with aegirine in Mn-1 and also occurs in Mn-2 representing the mineralized Mn cycle (Fig. 10). The principal reasons for this viewpoint is that the system acts as a diagenetic cycle owing to the fact that in Mn-1 an active oxide surface catalyst is likely responsible for the mineral assemblage, as opposed to enzymatic Mn oxidation. The interpretation is that braunite formation is due to combined diagenesis, as the segregated silica needed for braunite is typical of Fe system diagenesis. The most likely formation of braunite is sedimentary or early diagenetic via biogeochemically mediated processes, as proposed by Serdyuchenko (1980) and Johnson et al. (2016). These studies report scenarios that are broadly similarly to our Urucum samples. Micro-textural evidence (Figs. 11 and 12) clearly shows the formation of braunite in the vicinity of hematite biomat, vernadite/hollandite, and apatite, via the consumption of segregated silica. While syngenetic mineralization took place under oxic neutrophilic conditions, slightly alkaline and oxic conditions were also reported for braunite formation (pH 9.5–9.9; Eh + 0.43 V; Listova, 1961); this comports well with our scenario.

Serandite, as an oxide-silicate mineral, also belong to this process (empirical composition of hollandite also can contain Si). The relationship between serandite and braunite is documented by our Raman profiles (Fig. 10). Jacobsite can be interpreted as the transitional form between Mn and Fe oxides.

6.4. Diagenesis of other minerals

After cell death and decomposition, as well as breakdown of extracellular polymeric substance, ions that were previously bound on their surfaces release Ca, Mg, Na, K, P, S, Si, Co, Zn, Ba, Sr, and rare earth elements. These are bioactive elements in accordance with Takahashi et al. (2007), Heim (2010), Meyer et al. (2012), Gyollai et al. (2017), and Yu et al. (2019). Formation of CO_3^{2-}, PO_4^{2-}, SiO_4^{4-}, and SO_4^{2-} anions commences and a complex transforming mineralization begins to take place, which (depending on local geochemical conditions) can result in clay mineral formation, mixed carbonates, feldspar, silica, and apatite. These poorly crystallized minerals can transform into more stable minerals over time (Konhauser, 1998; Dupraz and Visscher, 2005). The various geochemical features of Mn ores are modulated by such syngenetic and diagenetic processes. These include increased Co content compared with crustal abundance, a characteristic for Urucum ores as well as the Úrkút locality (Polgári et al., 2012b; Biondi and Lopez, 2017). Reaction of FeOB with Co proceeds easily, and MnOB can also oxidize Cobalt (Moffett, 1990). The liberalization of the cell surface-bound elements provides sources of elements e.g., in the case of K in the formation of hollandite or Si in the case of braunite and other elements (Piacentini et al., 2013).

Abundant quartz is common in Mn-1, which in part is attributable to the contribution of detrital debris, but also represents the dominant segregated reactive silica phase (Cole and Shaw, 1983; Fisk et al., 2006). In laboratory experiments, FeOB requires protection against concentration and other types of stress, and silica is used for protection by microbes (Młoszewska et al., 2018). The amorphous silica can easily transform into more stable minerals, such as quartz (Herdianita et al., 2000).

In unit Mn-1, a part of the segregated silica is stabilized as quartz, but the formation of aegirine and braunite also consumed considerable amounts. Through combined diagenesis in Mn-2 and Mn-3, braunite and serandite formed, which consumed (and thus, reduced) the segregated silica content.

Feldspar and kaolinite/dickite also formed, and rarely, cancrinite occurs. Kaolinite minerals can form under acidic condition (pH 2–7) and within a wide temperature range. In our Urucum samples, only kaolinite and dickite were detected in this class of minerals. Kaolinite

can form at low temperatures 25 °C (Dekoninck et al., 2018). Dickite typically forms under low pH conditions. that forms in the temperature range between 120 and 280 °C (Eberl and Hower, 1975; Inoue, 1995), and its presence is not supported by our results, which favor low-temperature conditions. On the other hand, the reported important role of organic matter in the formation of dickite fits with our results (Maliva et al., 1999). Similar to the Al demand of chamosite mentioned above, the mobility of aluminum is enhanced by complexation with organic acids. In such systems, aluminum is released and hence available for clay-mineral precipitation when the organo-aluminum complexes are destabilized (Maliva et al., 1999).

Cancrinite is a mixed silicate-carbonate-sulfate transitional mineral, which only sporadically occurs in Urucum, but nevertheless reflects the variability of diagenetic conditions. Apatite can precipitate at pH of 7–8 and occurs in micrometer-sized crystals in the silica-rich part of BIFs. Similar apatite occurrences were noted in our samples, based on Raman and CL analyses. Muscovite (hydromuscovite) is common in the studied samples and was most likely formed by the diagenesis of cyanobacteria filaments in Fe-rich microbialites by the leaching of biofilm alkali elements (Na, Ka, Al, Mg) (Ewers, 1983; Gyollai et al., 2015,2017).

Among carbonates, the occurrence of dolomite (ankerite) in Mn-1 can be considerable, and strontianite is present but scarce. Barite, gypsum, and johannite belong to the sulfates that form from marine sulfate and/or organic constituents. Barite, a mineral precipitating under typical oxic conditions (Eh > +0.2) at low temperature, is considered here as oxygen supply indicator, because barite occurring with hematite indicates conditions that are more oxic than occurring without hematite (Hanor, 2000).

Considering the mineral assemblage, it is clear that the initially high segregated silica content did not support clay formation via early diagenesis, and silica-consuming minerals are numerous, which finally resulted in a decrease in silica content, which did not support quartz formation. In Mn-1, the quartz content is considerable compared with Mn-2 and Mn-3, which can be interpreted by the lower amount of Mn oxyhydroxides in Mn-1. Some quartz is probably of clastic origin as well as feldspar and mica, but authigenic formation of these minerals is also common in microbially mediated diagenetic processes, and non-luminescent minerals belong to this group (Marshall, 1998; Hassouta et al. 1999) (Fig. 7).

The Mn-2 and Mn-3 beds represent real enzymatic Mn(II) oxidation with extremely high amounts of Mn oxides and hydroxides, which overwhelm microbial Fe oxidation.

Most of the minerals detected here have well characterized formation conditions, as summarized in Table 4. Based on mineralogy, proto-ore sedimentation and diagenesis occurred under suboxic-obligatory to oxic and semi-neutral to alkaline conditions.

6.5. Formation of kremydilites and oblate structures

Kremydilites occur in varied forms shown in Fig. 4A, C, E, G, I and K, which probably correspond to different stages of development or growth. The presence of oblate structures and pores inside and outside the kremydilites indicate that they and the sediments in which they formed were a highly soft, porous, and permeable aqueous mud, within which pore fluids and gases could form and migrate out (Fig. 4A-B, E-F, G-H and Fig. 16). Gas bubbles are common accompanying phases of microbial mediation, which are trapped after burial, which is also characteristic of our Urucum samples (Fig. 4A-B, E-F, and G-H). Different stages of the formation of a kremydilite, including oblate structures, are shown in Fig. 4. The beginning of the microbial activity inside the aqueous mud deposited in the marginal basin floor, composed mainly of birnessite, ferrihydrite, organic matter, and Mn and Fe oxides (Fig. 8). Organic matter becomes oxidized (Fig. 4) generating CO_2 and/or CH_4 and/or H_2, which forms intergranular bubbles (Fig. 4A-B, E-F, and G-H) that migrate towards the surface (Fig. 16B). After the first oxidation stage of organic matter, a cluster of pores remains, constituting the nucleus zone of the kremydilite structures (Fig. 4A-B and C-D). The reactivation of microbial oxidation of organic matter generates the first concentric layer of pores (=shell) around the previously formed nucleus (Fig. 4E-F). The repetition of this process can generate multiple concentric layers of pores (shells) (Fig. 4G-H), and evolve to form a complex kremydilite (Fig. 4 I-J) with many layers, marked by the accumulation of pores concentrically organized around the nucleus, as in the kremydilite sample 48 (Fig. 4K and 8A-B). The reactivation process of microbial oxidation can cease at any time, forming kremydilites with one or two concentric layers around the nucleus or repeating at different times, forming complex structures with multiple concentric layers (Fig. 4I-J and K). The oblate structures, now preserved in the Urucum ores, did not reach the basin floor and were preserved during diagenesis. The cryptomelane needle mesh structure, the prismatic cryptomelane crystallites, and the micro-nodules were microbialites or organominerals (Dupraz et al. 2009), and the cylindrical holes are likely tube escape structures through which gas bubbles migrated from the zone of microbial activity (organic matter oxidation).

The mineralogy of the kremydilite from sample 48 (Fig. 8C-E) seems to reflect the changes caused by the diagenesis of the original sediment while it was buried (Fig. 16), as defined by Raiswell (1987). Burial initiated the diagenesis and ore formation (Fig. 8C-D and 16B) simultaneously with successive cycles of heterotrophic microbial activity, which formed the kremydilite concentric layers of cryptomelane, birnessite, ferrihydrite, rhodochrosite crystallized in the nucleus zone, braunite, rhodochrosite, cryptomelane crystallized in the bottom part, and ferrihydrite and cryptomelane in the upper part (Fig. 8C-D, and Fig. 16B). The complete oxidation of the layer and of all the kremydilites contained therein, forming the massive Mn-2 and 3 ore type, is a process that began during early diagenesis and was extended after lithification through microbial mediation. The origin of the oblate form of kremydilites, with concentric layers around a nucleus, is a consequence only of the oxidation of the organic matter (biomass) during diagenesis and the subsequent formation of pores. This process is independent of the chemical and/or mineral composition of the original sediment (but Mn reduction occurs). The original and present chemical and mineral composition of kremydilites arises from: (a) the abundant sedimentation of Mn oxyhydroxides via enzymatic oxidation and, to a lesser extent, of Fe oxyhydroxides and (b) the changes caused by diagenesis, which transforms the sediment into different minerals, as manganese (Fe-)-rich biomass becomes manganese-rich sediment, then Mn(Fe)-rich sedimentary rock. This is the origin of an economical Mn ore deposit. The absence of iron kremydilites in the jaspilites, similar to the Mn ore beds, shows that the formation of kremydilites was a unique process that only occurred in the Mn-rich sediments, forming a new type of manganese ore.

It was previously proposed that kremydilite formed by photoferrotroph microbial processes (photosynthetic) under anoxic conditions (Biondi and Lopez, 2017), which is not in accordance with the interpretation of recent results on the mineral assemblage. Our new interpretation is that these formed in suboxic-oxic conditions and slightly alkaline pH. To reach a plausible interpretation, as a first step, it is important to determine the formation processes of kremydilite. The mineral assemblage of the studied sample supports an early diagenetic origin, rather than syngenesis (Fig. 8). The kremydilite structure resembles both nodules and concretions; thus, to compare these structures, definitions are necessary. Nodules and concretions are very similar, and sometimes, these terms are used interchangeably. However, while concretions incorporate material of the host sediment, nodules contain solely authigenic phases (Raiswell and Fisher, 2000; Jackson, 2005; Baumann et al., 2016; and references therein). In our case, there are only authigenic minerals based on mineral assemblage in kremydilite and in oblate structures. Consequently, based on definition, these cannot be concretions but instead are most probably better termed nodules. The definition of a nodule is also contradictory in our case, however, as in sedimentology and geology terminology a nodule is

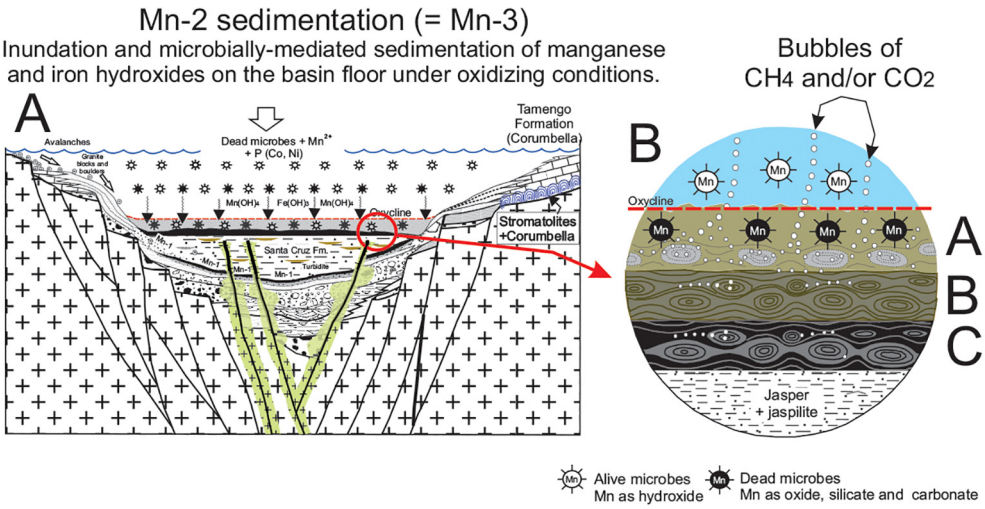

Zone	Sediment zones	Diagenetic product	Kremydilite growth
A	**Biomass sedimentation** Aqueous biomass mud with dead microbes. Mn reduction and carbonate nucleation	Microbial oxidation of buried organic matter under suboxic conditions	Birnesite and ferrihydrite nucleation, CM decay and formation of CH_4 and/or CO_2 bubbles
B	**Biomass early diagenesis** Biomass with Mn and Fe hydroxides + manganoan carbonate	Birnesite, ferrihydrite, manganoan carbonate	Nucleous, ferrihydrite and braunite + rhodochrosite zones formation, Ch_4 + CO_2 bubbles
C	**Biomass late diagenesis = Ore formation** Mn and Fe oxidation and carbonate precipitation	Transformation to cryptomelane, braunite and minor rhodochrosite	Transformation to cryptomelane, braunite and minor rhodochrosite

Fig. 16. Kremydilite formation environment on the floor of the Urucum basin. (A) General environment schematically showing the formation of a layer such as Mn-2 or Mn-3. (B) Detail of "mud" or silica-clayey biomass sedimented on the basin floor (left side), showing the evolutionary stages that occur from sedimentation to late diagenesis (right side).

usually defined as a small, irregularly rounded knot, mass, or lump of a mineral or mineral aggregate that typically has a contrasting composition from the enclosing sediment or sedimentary rock (Jackson, 2005). This is not the case in Urucum. In general, the objects we dub "nodules" lack any internal structure except for the preserved remnants of original bedding or fossils, which is also not the case here, as kremydilite is a concentric structure (structured pore system forming "pore shells" without cement infilling, which is also a difference). A further aspect is mineralogy, which differs from the typical ones occurring in nodules and concretions including most commonly calcite, siderite, chert, apatite (phosphorite), anhydrite, and pyrite. In Urucum, kremydilite occurs as high-quality Mn oxide ore.

Hence, based on the above definitions and features, kremydilite could be considered as a unique concretion-like structure, which lacks the background sediment, and the accumulated sediment is the result of successive phases of oxidation of organic matter (Fig. 4) during diagenesis (Fig. 8). Authigenic mineral formation occurs during syngenesis and early diagenesis. In this sense, kremydilite, the most characteristic structure in Mn-2 and Mn-3 ore beds, can be interpreted as a unique type of syngenetic and diagenetic structure and represent a unique type of ore (also taking into consideration Maynard (2010) and Kuleshov (2011), on ore types). This interpretation is further in accordance with the main features of kremydilites, like variable-preserved porous content, signs of gas production and migration, concentric structures, and the multiple stages of development. Then again, differences, such as lack of cementation and incorporation of material of the host sediment, are consequential. All things considered, this is a rare ore-type, as reported by Biondi and Lopez (2017).

Yet, how did these kremydilite structures form *en masse*? The interpretation that we favor is that heterotrophic cell colonies randomly activated in the microbialite sediment after burial in suboxic neutral/alkaline conditions, side-by-side with lithification and stabilization of minerals (Mn reduction (MnR) and reactive organic matter decomposition via heterotrophic microbial mediation can be referred to as Cycle II). Rhodochrosite is a common (dominant) component in the kremydilite structure in the core zone and also in the shells, from the core to the margin (Fig. 8). The process probably continues only along the poorly crystallized reactive vernadite and todorokite. Cryptomelane and braunite are more stable. They do not take part in the process, nor does ferrihydrite, as the system does not reach the Fe reduction zone (FeR) because of the high Mn concentration and relatively low organic matter content.

Why is Urucum (Neoproterozoic, Brazil) concretionary and not laminated like in Úrkút (Mesozoic, Hungary)? Much less organic matter was buried, and this fact did not lead to the formation of a horizontally continuous MnR zone realizing rhodochrosite laminae. Instead, local heterotrophic cell colony centers caused the formation of kremydilite in the biomat system, overprinting the syngenetic lamination, causing a nodular, concretional appearance. The kremydilites are most probably diagenetic and not syngenetic, as rhodochrosite is diagenetic, as referred to in Polgári et al. (2012b), Maynard (2014), and Johnson et al. (2016).

Both FTIR and RAMAN analyses show that substances inside and outside the oblate structures evolved in different ways. This is

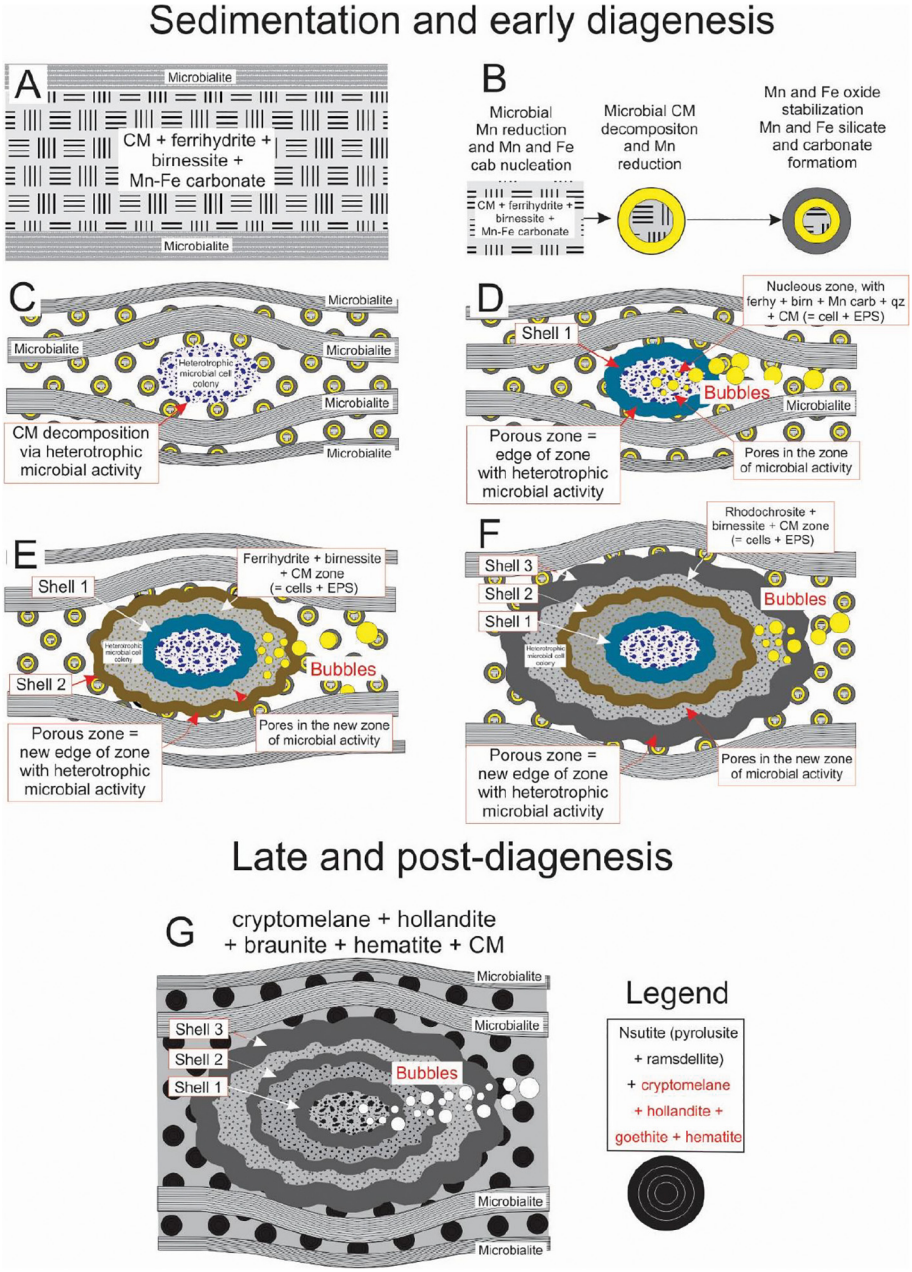

Fig. 17. Cartoon showing the processes of formation of the micro-nodules, oblate structures, kremydilites, and the massive manganese ore of the Mn-2 and Mn-3 layers of Urucum. Abbrev.: CM-organic matter. Read text for details.

exemplified by the presence of pores in each kremydilite shell, the absence of pores inside the bubbles, and the absence of micro-nodules inside the oblate structures. At the contact zone of the "more" oxic outer part and "suboxic" inner part, spherical enrichment of cryptomelane occurred, forming a dense margin (rim). The micro-texture of this rim (and also the outer and inner part) is microbial and contain "diffusional channels" (SI 11-Fig).

6.6. Basin development

As mentioned, unit Mn-1 follows the basin floor relief, while Mn-2 and Mn-3 occur as horizontal beds in the ironstone. This can be viewed as a special series produced by syngenetic processes via authigenic mineral accumulation, summarized according to chronology of syngenetic and diagenetic processes in Fig. 17. The ore formation commenced with flooding on porous fluvial sediments, and the ore forming fluids (Fe^{2+} and Mn^{2+}) infiltrated and microbially colonized the pores in a woven form, and around the clastic particles in the sediment to the depth where diffusion was active (supported by microbially mediated micro-texture, which is syngenetic). Initially, biomass, composed of Mn and Fe hydroxides, organic matter, manganoan and ferroan carbonate and amorphous silica, deposited on the basin floor. In the extracellular polymeric substance network, diagenetic minerals along with clastic material dominated (based on CL). The ore formation started with enzymatic Fe oxidation, as the Raman profiles of Mn-1 samples prove, resulting in a well-developed biomat system. This offered oxide surface catalysis for Mn oxidation, which was not enzymatic during Mn-1 because the level of oxygen supply did not reach the obligatory oxic level (Morgan, 2005). The dynamic processes affected the top zone of sediments up to the diffusion depth, which moved upward in time, forming the Mn-1 ore bed.

The effect of fluvial contribution decreased via marine flooding, and

the clastic contribution ceased gradually, offering excellent calm conditions for undisturbed Fe- and Mn-biomat formation, resulting in fine cyclic mineral lamination (mineralized biomats, microbialite) (Fig. 10, SI 12-Fig). The FeOB continued forming ironstone (Biondi and Lopez, 2017), under suboxic conditions, in which oxygen supply was not favorable for MnOB.

Enzymatic Mn oxidation starting as chemical nutrients (Mn^{2+}) were in the system, and the Mn-2 and later Mn-3 layers suddenly occurred in the Fe sediments. This made conditions more oxic and obligatory oxic. The sudden change is caused simply by the turning of oxygen supply from suboxic (dissolved oxygen-DO 0.2–2.0 mL/L) to obligatory oxic (DO > 2.0 mL/L) conditions, which is the *criterion* of enzymatic Mn(II) oxidation. In the background of formation of Mn-2 and Mn-3, the microbial Fe oxidation continued, as supported by the well detectable micro-lamination (cyclicity) of microminerals. The sharp contact in the field representing that horizon where Fe is forced back to local suboxic parts. The Fe^{2+} ascending fluid does not reach the obligatory oxic zone as a dominant contribution, because microbes oxidize it in the suboxic zone (Fig. 15). The Raman profiles clearly show that the Fe biomat system existed via all Mn ore beds, but with different intensity. Fe and Mn occurred together in an intimate form similar to Úrkút (Polgári et al. 2012b). A similar sharp boundary (contact zone) occurs between gray (black) shale and Mn carbonate ore in Úrkút, which is also the result of change in the oxygen supply becoming obligatory oxic. This was a sensitive redox system for enzymatic Mn oxidation (Polgári et al., 2016a).

Summarizing the ore formation, Fig. 17 shows our model for the process that generated the massive manganese ore with kremydilites, found in the Mn-2 and Mn-3 layers of Urucum. After the formation of the ferrihydrite, birnessite, organic matter, and rhodochrosite mud-like biomass (Fig. 17A), the microbial reduction generates micro-nodules with the minerals of the original sediment in the nucleus involved by ferrihydrite (Fig. 17B), then by rhodochrosite and braunite. Late diagenetic and post-diagenetic oxidation generates Mn-2 and Mn-3 ore layers, composed of massive and/or zoned, concentric, spherical nodules, and/or zoned nodules with an eye shape (Fig. 17C). The formation of kremydilites begins simultaneously or immediately after the formation of micro-nodules, in places where a cluster of microbes begins to oxidize organic matter, generating pores and producing methane, CO_2, and/or H_2 bubbles. This activity forms a small structure with a homogeneous and porous nucleus bound by a porous layer, which may involve the nucleus totally or partially, formed at the edge of the zone of microbial activity. The resumption of microbial activity around the same nucleus will cause greater oxidation where a greater amount of non-oxidized organic matter is available, generally near and on the outside of the last formed layer.

Late and post-diagenetic processes cause complete oxidation of the micro-nodules and kremydilites (Fig. 17D). Raman analyses of spherical nodules of sample 75-B2 show that central parts of micro-nodules were transformed to hollandite/vernadite and organic matter, around which cryptomelane and nsutite (pyrolusite and ramsdellite) crystallize (Fig. 17F). The minerals of the kremydilites are entirely oxidized during post-diagenetic conditions and transformed mainly into cryptomelane, hollandite, braunite, with little organic matter, hematite and goethite, generating the massive manganese ore of the Urucum and Mn-2 and Mn-3 layers (Fig. 17G). From time to time, coarse detrital influx disturbed the calm formation of microbial mats, resulting in turbiditic accumulation. It has been proposed that these turbidites were caused by earthquakes from rifting activity (Biondi and Lopez, 2017). The most probable source of ore was hydrothermal, exhalative in submarine environment (Biondi and Lopez, 2017 and references therein).

7. Conclusions

High-resolution Raman and AT-FTIR spectroscopy used on Mn ore samples of Mn-1, Mn-2, and Mn-3 ore beds in the ca. 550 Ma Urucum deposit yields information used to construct a self-consistent model for the formation of these ores. This approach was used to document numerous metastable, poorly crystallized mineral phases and organic matter that represent the remnants of primary microbially mediated Mn and Fe minerals.

1. Based on mineralogy, the proto-ore sedimentation and the diagenesis of the Urucum Mn ore deposit occurred under suboxic-obligatory oxic and semi-neutral to alkaline conditions, where microbial Mn^{2+} enzymatic oxidation (with reactive organic matter) resulted in fine-grained accumulation of Mn oxides (Cycle I).
2. The sharp contact between the manganese and iron layers represents that horizon, where the obligatory oxic conditions facilitated the start of enzymatic Mn oxidation (Mn engine), which overwhelmed microbial Fe oxidation. The Fe biomat system existed via all Mn ore beds, but with different intensity. Fe and Mn occurred together in an intimate form.
3. Heterotrophic microbially mediated Mn reduction (Cycle II) developed only locally embedded in the form of oxide kremydilite structure, which represents a unique, new ore type. Among the kremydilite structures, regular double-microbial mineralogical cycles formed with alternating mineralized Fe- and Mn-oxidizing bacterial activity (microbialite). Detailed study raised that kremydilite and oblate structures formed on the effect of heterotrophic cell colonies, whose activity overprinted the original lamination. The Mn reduction resulted in rhodochrosite (Cycle II) a characteristic constituent in these structures. The reason that rhodochrosite formation did not become dominant in the form of laminae is the smaller amount of organic matter accumulation, which allowed for Mn reduction via diagenesis only in random centers, resulting in diagenetic kremydilite. That is why oxic-suboxic mineral stabilization and diagenetic mineral formation became dominant.
4. Mn-1 follows the basin floor relief, whereas Mn-2 and Mn-3 occur as horizontal beds in the ironstone pile. The ore formation started with flooding on porous fluvial sediments, and the ore forming fluids (Fe^{2+} and Mn^{2+}) infiltrated and microbially colonized the pores in a woven form, and around the clastic particles on chemical (Fe^{2+}, Mn^{2+}) nutrients, in the sediment to the depth where diffusion was active. In the extracellular polymeric substance network, diagenetic minerals along with clastic material became dominant.
5. The Fe-oxidizing bacteria continued forming ironstone, under suboxic conditions, in which oxygen supply was not favorable for Mn-oxidizing bacteria.
6. From time to time, coarse detrital influx disturbed the calm biomat formation, resulting in clast accumulation, which interrupted the fine microbial lamination. These turbidites may have been caused by earthquakes (due to rifting activity).

Conflict of interest

The authors declare no competing financial interests on this research. The research in this manuscript has not been previously published nor is under consideration elsewhere. All authors have approved submission of this manuscript to *Precambrian Research*.

Acknowledgments

The authors thank the support of National Research, Development and Innovation Office, National Scientific Research Found No. 125060. We also thank the Companies VALE URUCUM and MCR URUCUM, for allowing us access to their mines and allowing the collection of samples of their ores. S.J.M. thanks the CNRS-CRPG, Nancy and the University of Lorraine (France) for a visiting professorship appointment during the writing phase of this paper. Comments by anonymous reviewers, as well as editorial handling by Wilson Teixeira and Eric Tohver are appreciated.

Appendix A. Supplementary data

Supplementary data to this article can be found online at https://doi.org/10.1016/j.precamres.2020.105624.

References

Almeida, F.F.M., 1946. Origem dos minérios de ferro e manganês de Urucum (Corumbá, Estado do Mato Grosso): Boletim da Divisão de Geologia e Mineralogia do Departamento Nacional da Produção. Mineral (DNPM, Rio de Janeiro) 119, 58p.

Angerer, T., Hagemann, S.G., Walde, D.H.G., Halverson, G.P., Boyce, A.J., 2016. Multiple metal source in glaciomarine facies of the Neoproterozoic Jacadigo iron formation in the "Santa Cruz deposit", Corumbá, Brazil. Precambr. Res. 275, 369–393.

Babinski, M., Boggiani, P.C., Fanning, C.M., Fairchild, T.R., Simo, C.M., Sial, A.N., 2008. U-Pb SHRIMP geochronology and isotope chemostratigraphy (C, O, S) of the Tamengo formation, Southern Paraguay Belt, Brazil. South American Symposyum on Isotope Geology, 6th, San Carlos de Bariloche (Argentina), p. 160.

Baele, J.M., Bouvain, F., De Jong, J., Matielli, N., Papier, S., Préat, A., 2008. Iron microbial mats in Modern and Phanerozoic environments. In Instruments, Methods, and Missions for Astrobiology XI (Vol. 7097, p. 70970N 12p.). International Society for Optics and Photonics.

Banfield, J.F., Nealson K.H. (eds), 1997. Geomicrobiology: Interactions between Microbes and Minerals. Reviews in Mineralogy 35, Mineralogical Society of America, Washington, D.C.

Bargar, J.R., Tebo, B.M., Bergmann, U., Webb, S.M., Glatzel, P., Chiu, V.Q., Villalobos, M., 2005. Biotic and abiotic products of Mn (II) oxidation by spores of the marine Bacillus sp. strain SG-1. Am. Mineral. 90 (1), 143–154.

Baumann, L.M., Birgel, D., Wagreich, M., Peckmann, J., 2016. Microbially-driven formation of Cenozoic siderite and calcite concretions from eastern Austria. Austrian J. Earth Sci. 109 (2), 211–232.

Bazylinski, D.A., Frankel, R.B., 2003. Biologically controlled mineralization in prokaryotes. In: Dove P.M., De Yoreo J.J. and Weiner S. (eds), Biomineralization, Reviews in Mineralogy and Geochemistry 54, Mineralogical Society of America and the Geochemical Society, Washington, D.C.

Bengtson, S., 2002. Origins and early evolution of predation. Paleontological Society papers 8, 289–317.

Berner, R.A., 1980. Early diagenesis: a theoretical approach 250 Princeton University Press, Princeton.

Biagioni, C., Capalbo, C., Lezzerini, M., Pasero, M., 2014. Ferrihollandite, $BaMn_6^{4+}Fe_2^{3+}O_{16}$, from Apuan Alps, Tuscany, Italy: description and crystal structure. Eur. J. Mineral. 26, 171–178.

Biondi, J.C., Lopez, M., 2017. Urucum Neoproterozoic-Cambrian manganese deposits (MS, Brazil): Biogenic participation in the ore genesis, geology, geochemistry, and depositional environment. Ore Geol. Rev. 91, 335–386.

Bodeï, S., Manceau, A., Geoffroy, N., Baronnet, A., Buatier, M., 2007. Formation of todorokite from vernadite in Ni-rich hemipelagic sediments. Geochim. Cosmochim. Acta 71 (23), 5698–5716.

Chan, C.S., Fakra, S.C., Emerson, D., Fleming, E.J., Edwards, K.J., 2011. Lithotrophic iron-oxidizing bacteria produce organic stalks to control mineral growth: implications for biosignature formation. Multidisciplinary Journal of International Society for Microbial Ecology 5, 717–727.

Chen, J.Y., Schopf, J.W., Bottjer, D.J., Zhang, C.Y., Kudryavtsev, A.B., Tripathi, A.B., Wang, X.Q., Yang, Y.H., Gao, X., Yang, Y., 2007. Raman spectra of a Lower Cambrian ctenophore embryo from southwestern Shaanxi, China. Proc. Natl. Acad. Sci. 104 (15), 6289–6292.

Chilingar, G.V., Buryakovsky, L.A., Eremenko, N.A., Gorfunkel, M.V., 2005. Geology and Geochemistry of Oil and Gas. Developments in Petroleum Science 52, 138–142.

Chumakov, N.M., 2009. The Baykonurian glacio-horizon of the Late Vendian. Stratigr. Geol. Correl. 17 (4), 373–381. https://doi.org/10.1134/S0869593809040029.

Chumakov, N.M., 2011. Glacial deposits of the Baykonur Formation, Kazakhstan and Kyrgyzstan. Geological Society, London, Memoirs Chapter 26, 36(1): 303-307.doi: 10.1144/M36.26.

Cole, T.G., Shaw, H.F., 1983. The nature and origin of authigenic smectites in some recent marine sediments. Clay Miner. 18, 239–252.

Coleman, M.L., 1985. Geochemistry of diagenetic non-silicate minerals: kinetic considerations. Philos. Trans. R. Soc. Lond. A315, 39–56.

Costa, M.L., Fernandez, O.J.C., Ribeiro, P.A., Silva, N.C., Poellmann, H., 2005. Contribuições mineralógicas e geoquímicas sobre a origem do minério de manganês do Morro do Urucum (Corumbá, Brasil): Simpósio Brasileiro de Metalogenia, 1th, Gramado (RS, Brasil). Abstracts, CDROM.

Dardenne, M.A., 1998. Modelo hidrotermal exalativo para os depósitos de Fe-Mn da região de corumbá, Mato Grosso do Sul: Congresso Brasileiro de Geologia, 40th, São Paulo, Brasil, Abstracts, p. 158.

Davies, S.H., Morgan, J.J., 1989. Manganese (II) oxidation kinetics on metal oxide surfaces. J. Colloid Interface Sci. 129 (1), 63–77.

Decarreau, A., Petit, S., Martin, F., Farges, F., Vieillard, P., Joussein, E., 2008. Hydrothermal synthesis, between 75 and 150°C, of high-charge, ferric nontronites. Clays Clay Miner. 56 (3), 322–337.

Decarreau, A., Petit, S., Vieillard, P., Dabert, N., 2004. Hydrothermal synthesis of aegirine at 200 C. Eur. J. Mineral. 16 (1), 85–90.

Dekoninck, A., Moussi, B., Vennemann, T., Jamoussi, F., Mattielli, N., Decrée, S., Chaftar, H.-R., Hatira, N., Yans, J., 2018. Mixed hydrothermal and meteoric fluids evidenced by unusual H- and O-isotope compositions of kaolinite-halloysite in the Fe(-Mn) Tamra deposit (Nefza district, NW Tunisia). Appl. Clay Sci. 163, 33–45. https://doi.org/10.1016/j.clay.2018.07.007.

Dorr, J.V.N., 1945. Manganese and iron deposits of Morro do Urucum, Mato Grosso, Brazil: United States Geological Survey. Bulletin 946A, 47p.

Dupraz, C., Visscher, P.T., 2005. Microbial lithification in marine stromatolites and hypersaline mats. Trends Microbiol. 13, 429–438.

Dupraz, S., Parmentier, M., Ménez, B., Guyot, F., 2009. Experimental and numerical modeling of bacterially induced pH increase and calcite precipitation in saline aquifers. Chem. Geol. 265, 44–53.

Eberl, D., Hower, J.O.H.N., 1975. Kaolinite synthesis: The role of the Si/A1 and (alkali)/(H+) ratio in hydrothermal systems. Clays Clay Miner. 23, 301–309.

Ehrenreich, A., Widdel, F., 1994. Anaerobic oxidation of ferrous iron by purple bacteria, a new type of phototrophic metabolism. Appl. Environ. Microbiol. 60 (12), 4517–4526.

Ehrlich, H.L., 2002. Geomicrobiology, 4th ed. Marcell Dekker Inc., pp. 183–274.

Ewers, W.E., 1983. Chemical Factors in the Deposition and Diagenesis of Banded Iron-Formation. In: Trendall, A.F., Morris, R.C. (Eds.), Developments in Precambrian Geology 6, Iron formation: Facts and Problems. Elsevier, pp. 491–512.

Fisk, M.R., Popa, R., Mason, O.U., Storrie-Lombardi, M.C., Vicenzi, E.P., 2006. Iron-magnesium silicate bioweathering on Earth (and Mars?). Astrobiol. 6 (1), 48–69.

Fortey, N.J., Michie, U.M., 1978. Aegirine of possible authigenic origin in Middle Devonian sediments in Caithness, Scotland. Mineral. Mag. 42 (324), 439–442.

Frei, R., Døssing, L.N., Gaucher, C., Boggiani, P.C., Frei, K.M., Bech, Árting T., Crowe, S.A., Freitas, B.T., 2017. Extensive oxidative weathering in the aftermath of a late Neoproterozoic glaciation – Evidence from trace element and chromium isotope records in the Urucum district (Jacadigo Group) and Puga iron formations (Mato Grosso do Sul, Brazil). Gondwana Res. 49, 1–20.

Freitas, B.T., Warren, L.V., Boggiani, P.C., Paes de Almeida, R., Piacentini, T., 2011. Tectono-sedimentary evolution of the Neoproterozoic BIF-bearing Jacadigo Group, SW Brazil. Sedimentary Geology 238, 48–70.

Garrels, R.M., MacKenzie, F.T., 1971. Evolution of Sedimentary Rocks. Nortom, New York.

Germs, G.J.B., 1972. New y fossil from Nama Group, South West Africa. American Journal of Sciences 272, 752–761.

Germs, G.J.B., Gaucher, C., 2012. Nature and extent of a late Ediacaran (ca. 547 Ma) glaciogenic erosion surface in southern Africa. S. Afr. J. Geol. 115, 91–102. https://doi.org/10.2113/gssajg.115.91.

Giovanoli, R., 1980. On natural and synthetic manganese nodules. In: Varentsov, I.M., Grasselly, Gy. (Eds.), Geology and Geochemistry of Manganese. 1. Akadémiai Publishing House, Budapest, pp. 159–203.

Götze, J., Plötze, M., Götte, T., Neuser, R.D., Richter, D.K., 2002. Cathodoluminescence (CL) and electron paramagnetic resonance (EPR) studies of clay minerals. Mineral. Petrol. 76 (3–4), 195–212.

Graf, J.L., O'Connor, E.A., Leeuwen, P.V., 1994. Rare earth element evidence of origin and depositional environment of late Proterozoic ironstone beds and manganese ore deposits, SW Brazil and SE Bolivia. Journal of South American Earth Sciences 7, 115–133.

Grant, S.W.F., 1990. Shell structure and distribution of Cloudina, a potential index fossil for the terminal Proterozoic. American Journal of Sciences 290, 261–294.

Grotzinzer, J.P., Bowring, S.A., Saylo, B.Z., Kaufman, A.J., 1990. Biostratigraphic and geochronology constraints on early animal evolution. Science 270, 598–604.

Gyollai, I., Polgári, M.P., Fintor, K., Popp, F., Mader, D., Pál-Molnár, E., 2015. Microbially mediated deposition of postglacial transition layers from the Neoproterozoic Otavi Group, Namibia: evidence of rapid deglaciation after the Sturtian cryogenic period. Carpathian Journal of Earth and Environmental Sciences 10 (1), 63–76.

Gyollai, I., Polgári, M., Fintor, K., Pál-Molnár, E., Popp, F., Koeberl, C., 2017. Microbial activity records in Marinoan Snowball Earth postglacial transition layers connecting diamictite with cap carbonate (Otavi Group, NW-Namibia). Austrian J. Earth Sci. 110 (1), 2–18.

Hallbeck, L., Pedersen, K., 1990. Culture parameters regulating stalk formation and growth rate of Gallionella ferruginea. Microbiology 136 (9), 1675–1680.

Hanor, J.S., 2000. Barite-celestine geochemistry and environments of formation. Rev. Mineral. Geochem. 40, 193–275.

Haralyi, N.L.E., Walde, D.H.G., 1986. Os minerais de ferro e manganês da região de Urucum, Mato Grosso do Sul, in Schobenhaus, C., and Coelho, C.E.S., ed., Principais Depósitos Minerais do Brasil. Departamento Nacional da Produção Mineral (Brasilia, Brazil) 2, 127–144.

Harder, H., 1976. Nontronite synthesis at low temperatures. Chem. Geol. 18 (3), 169–180.

Harder, H., 1978. Synthesis of iron layer silicate minerals under natural conditions. Clays Clay Miner. 26 (1), 65–72.

Hassouta, L., Buatier, M.D., Potdevin, J.L., Liewig, N., 1999. Clay diagenesis in the sandstone reservoir of the Ellon Field (Alwyn, North Sea). Clays Clay Miner. 47 (3), 269–285.

Heim, C.N., 2010. An integrated approach to the study of biosignatures in mineralizing biofilms and microbial mats. PhD thesis, Georg-August-University of Göttingen Germany, 183.

Herdianita, N.R., Browne, P.R.L., Rodgers, K.A., Campbell, K.A., 2000. Mineralogical and textural changes accompanying ageing of silica sinter. Miner. Deposita 35, 48–62.

Hofmann, H.J., Mountjoy, E.W., 2001. Namacalathus-Cloudina assemblage in Neoproterozoic Miette Group (Byng Formation), British Columbia – Canada oldest shelly fossil. Geology 29, 1091–1094.

Inoue, A., 1995. Determination of aspect ratios of clay-sized particle. Clay Science 9 (5), 259–274.

Jackson, J.A., 2005. Glossary of geology, 5th revised and enlarged ed. Springer, Berlin, pp. 900 ISBN 3-540-27951-2.

Jehlička, J., Šťastná, A., Přikryl, R., 2009. Raman spectral characterization of dispersed carbonicaceous matter in decorative crystalline limestones. Spectrochim. Acta Part A

Mol. Biomol. Spectrosc. 73 (3), 404–409.
Johnson, J.E., Webb, S.M., Ma, C., Fischer, W.W., 2016. Manganese mineralogy and diagenesis in the sedimentary rock record. Geochim. et Cosmochim. Acta 173, 210–231.
Klein, C., Ladeira, E.A., 2004. Geochemistry and mineralogy of Neoproterozoic banded iron-formations and some selected, siliceous manganese formations form the Urucum district, Mato Grosso do Sul, Brazil. Econ. Geol. 99, 1233–1244.
Konhauser, K.O., 1998. Diversity of bacterial iron mineralization: Earth-Science Revs. 43, 91–121.
Kuleshov, V.N., 2011. Manganese deposits: Communication 1. Genetic models of manganese ore formation. Lithol. Min. Resour. 46, 473–493. https://doi.org/10.1134/S0024490211050038.
van Leeuwen, P., Graaf, J.L., 1987. The Urucum-Mutum iron and manganese deposits, Mato Grosso do Sul, Brazil, and Santa Cruz, Bolivia. Part 1-The region's potential as an economic source of iron and manganese. Geol. Mijnbouw 65, 317–325.
Leonardos, O.H., Walde, D.H.G., 1982. Sobre a estratigrafia e a gênese dos depósitos de manganês a luz do vulcanismo Jacadigo: Congresso da Sociedade Brasileira de Geociências, 27th. Abstracts, Salvador, pp. 203.
Listova, L.P., 1961. Experimental studies of physic-chemical conditions of sedimentation of manganese oxides and carbonate. Ocherki Metallogen. Osadochn. Porod. Publication of the AN USSR, Moscow, pp. 319–351.
Maliva, R.G., Dickson, J.A.D., Fallick, A.E., 1999. Kaolin cements in limestones; potential indicators of organic-rich pore waters during diagenesis. J. Sediment. Res. 69 (1), 158–163.
Mandernack, K.W., Post, J., Tebo, B.M., 1995. Manganese mineral formation by bacterial spores of the marine Bacillus, strain SG-1: evidence for the direct oxidation of Mn (II) to Mn (IV). Geochim. Cosmochim. Acta 59 (21), 4393–4408.
Marshall, D.J., 1998. Cathodoluminescence of Geological Materials. Unwin Hyman, Boston, pp. 146.
Maynard, J.B., 1983. Geochemistry of Sedimentary Ore, Deposits. Ed. Springer Verlag, New York.
Maynard, J.B., 2010. The chemistry of manganese ores through time: a signal of increasing diversity of earth-surface environments. Econ. Geol. 105, 535–552. https://doi.org/10.2113/gsecongeo.105.3.535.
Maynard, J.B., 2014. Manganiferous sediments, rocks, and ores. Treatise on Geochemistry. Elsevier 327–349.
Meyer, E.E., Quicksall, A.N., Landis, J.D., Link, P.K., Bostick, B.C., 2012. Trace and rare earth elemental investigation of a Sturtian cap carbonate, Pocatello, Idaho: Evidence for ocean redox conditions before and during carbonate deposition. Precambr. Res. 192–195, 89–106.
Młoszewska, A.M., Cole, D.B., Planavsky, N.J., Kappler, A., Whitford, D.S., Owttrim, G.W., Konhauser, K.O., 2018. UV radiation limited the expansion of cyanobacteria in early marine photic environments. Nat. Commun. 9, 3088.
Moffett, J.W., 1990. Microbially meddiated cerium oxidation in sea-water. Nature 345 (6274), 421–423.
Morgan, J.J., 2005. Kinetics of reaction between O_2 and Mn (II) species in aqueous solutions. Geochim. Cosmochim. Acta 69 (1), 35–48.
Novick, A., 1955. Growth of Bacteria. Ann. Rev. Microbiol. 9, 97–110.
O'Connor, E.A., Walde, D.H.G., 1985. Recognition of an Eocambrian orogenic cycle in SW Brazil and Bolivia: Zbl. Geologie Paläontologie 1, 1441–1456.
Okolo, G.N., Neomagus, H.W., Everson, R.C., Roberts, M.J., Bunt, J.R., Sakurovs, R., Mathews, J.P., 2015. Chemical–structural properties of South African bituminous coals: Insights from wide angle XRD–carbon fraction analysis, ATR–FTIR, solid state 13C NMR, and HRTEM techniques. Fuel 158, 779–792.
Orange, D., Knittle, E., Farber, D., Williams, Q., 1996. Raman spectroscopy of crude oils and hydrocarbonic fluid inclusions: A feasibility study. The Geochemical Society, Special Publication 5, 65–81.
Parry, L.A., Boggiani, P.C., Condon, D.J., Garwood, R.J., Leme, J.M., McIlroy, D., Brasier, M.D., Trindade, R., Campanha, G.A.C., Pacheco, M.L.A.F., Cleber, Q.C., Diniz, C.Q.D., Alexander, G., Liu, A.G., 2017. Ichnological evidence for meiofaunal bilaterians from the terminal Ediacaran and earliest Cambrian of Brazil. Nature (Ecology and Evolution) 1(10), 1455–1464. https://doi.org/10.1038/s41559-017-0301-9.
Piacentini, T., Vasconcelos, P.M., Farley, K.A., 2013. $^{40}Ar/^{39}Ar$ constraints on the age and thermal history of the Urucum Neoproterozoic banded-iron formation, Brazil. Precambr. Res. 228, 48–62.
Polgári, M., Gyollai, I., 2019. Connection between biomineralization and the evolution of Earth. Front. Microbiol in press.
Polgári, M., Gyollai, I., Fintor, K., Horváth, H., Pál-Molnár, E., Biondi, J.C., 2019. Microbially mediated ore forming processes and the cell mineralization. Front. Microbiol in press.
Polgári, M., Hein, J.R., Tóth, A.L., Pál-Molnár, E., Vigh, T., Bíró, L., Fintor, K., 2012a. Microbial action formed Jurassic Mn-carbonate ore deposit in only a few hundred years (Úrkút, Hungary). Geology 4 (10), 903–906.
Polgári, M., Hein, J.R., Bíró, L., Gyollai, I., Németh, T., Sajgó, C., Fekete, J., Schwark, L., Pál-Molnár, E., Hámor-Vidó, M., Vigh, T., 2016a. Mineral and chemostratigraphy of a Toarcian black shale hosting Mn-carbonate microbialites (Úrkút, Hungary). Palaeogeogr. Palaeoclimatol. Palaeoecol. 459, 99–120.
Polgári, M., Hein, J.R., Németh, T., Pál-Molnár, E., Vigh, T., 2013. Celadonite and smectite formation in the Úrkút Mn-carbonate ore deposit (Hungary). Sed. Geol. 294, 157–163.
Polgári, M., Hein, J.R., Vigh, T., Szabó-Drubina, M., Fórizs, I., Bíró, L., Müller, A., Tóth, A.L., 2012b. Microbial processes and the origin of the Úrkút manganese deposit, Hungary. Ore Geol. Rev. 47, 87–109.
Polgári, M., Németh, T., Pál-Molnár, E., Futó, I., Vigh, T., Mojzsis, S.J., 2016b. Correlated chemostratigraphy of Mn-carbonate microbialites (Úrkút, Hungary). Gondwana Res. 29 (1), 278–289. https://doi.org/10.1016/j.gr.2014.12.002.
Putzer, H., 1958. Die Kryptomelan- und Jaspelit-Lagerstätten von Corumbá im Staate Mato Grosso. Brasilien: Erzmet all 11, 527–538.
Raiswell, R., 1987. Non-steady state microbial diagenesis and the origin of carbonate concretions and nodular limestones. In: J.D. Marshall (eds), Diagenesis of sedimentary sequences. London: Geological Society Spec Pub 36:41–54.
Raiswell, R., Fisher, Q.J., 2000. Mudrock-hosted carbonate concretions: a review of growth mechanisms and their influence on chemical and isotopic composition. Journal of the Geological Society 157 (1), 239–251.
Rajabzadeh, M.A., Haddad, F., Polgári, M., Fintor, K., Walter, H., Molnár, Z., Gyollai, I., 2017. Investigation on the role of microorganisms in manganese mineralization from Abadeh-Tashk area, Fars Province, southwestern Iran by using petrographic and geochemical data. Ore Geol. Rev. 80, 229–249.
Savko, K.A., 2006. Phase equilibria in rocks of the paleoproterozoic banded iron formation (BIF) of the Lebedinskoe deposit, Kursk Magnetic Anomaly, and the petrogenesis of BIF with alkali amphiboles. Petrology 14 (6), 567–587.
Schneider, G., 1984. Zur Mineralogie and Lagerstättenbildung der Mangan- und Eisenerzvorkommen de Urucum Distriktes (Mato Grosso, Brasilien): Frankfurter Geowiss. Arb. Serie C 1, (Frankfurt), p. 205.
Schreck, P., 1984. Geochemische Klassifikation und Petrogenese der Manganerze des Urucum Distriktes bei Corumbá (Mato Grosso do Sul. Brasilien): Frankfurter Geowiss. Arb. Serie C 1, (Frankfurt), 206 p.
Schwertmann, U., Cornell, R.M., 2007. Iron Oxides in the Laboratory: Preparation and Characterization. Wiley-VCH, pp. 188.
Serdyuchenko, D.P., 1980. Precambrian biogenic-sedimentary manganese deposits. In Geology and Geochemistry of Manganese, Vol. 2 (ed. I. M. Varentsov and G. Grasselly), Stuttgart, 61-88.
Skinner, H.C.W., 1993. A review of apatites, iron and manganese minerals and their roles as indicators of biological-activity in black shales. Precambr. Res. 61 (3–4), 209–229.
Straub, K.L., Benz, M., Schink, B., Widdel, F., 1996. Anaerobic, nitrate-dependent microbial oxidation of ferrous iron. Appl. Environ. Microbiol. 62 (4), 1458–1460.
Sung, W., Morgan, J.J., 1981. Oxidative removal of Mn (II) from solution catalysed by the γ-FeOOH (lepidocrocite) surface. Geochim. Cosmochim. Acta 45 (12), 2377–2383.
Takahashi, Y., Hirata, T., Shimizu, H., Ozaki, T., Fortin, D., 2007. A rare earth element signature of bacteria in natural waters? Chem. Geol. 244 (3–4), 569–583.
Trompette, R., Alvarenga, C.J.S., Walde, D.H.G., 1998. Geological evolution of the Neoproterozoic Corumbá graben system (Brazil) – Depositional context of the stratified Fe and Mn of the. Jacadigo Group: Journal of south American Earth Sciences 11, 587–597.
Trudinger, P.A., Swaine, D.J. eds., 1979. Biogeochemical cycling of mineral-forming elements (Vol. 3). Elsevier. pp. 1-672. http://oriasmail.citromail.hu/dl3/?tid=7aab706ea32020b3008ea46a063058758.
Tsikos, H., Moore, J.M., 2005. Sodic metasomatism in the Palaeoproterozoic Hotazel iron-formation, Transvaal Supergroup, South Africa: implications for fluid–rock interaction in the Kalahari manganese field. Geofluids 5 (4), 264–271.
Urban, H., Stribrny, B., Lippolt, H., 1992. Iron and manganese deposits of the Urucum district, Mato Grosso do Sul, Brazil. Econ. Geol. 87, 1375–1392.
Villalobos, M., Toner, B., Bargar, J., Sposito, G., 2003. Characterization of the manganese oxide produced by Pseudomonas putida strain MnB1. Geochim. Cosmochim. Acta 67 (14), 2649–2662.
Walde, D.H.G., 1981. Die Mangan- und Eisenvorkommen von Urucum, Mato Grosso, Brasilien: Erste Ergebnisse und ein weiteres Program. Zbl. Geol. Paläontologie 1, 505–513.
Walde, D.H.G., 1988. Das proterozoische Paraguay-Araguaia Orogen in West-Brasilien, Ausgehend von Untersuchungen im Raum Corumbá: Habilitationsscrift, Albert Ludwigs Universität, Freiburg, pp. 122 (unpublished).
Walde, D.H.G., Gierth, E., Leonardos, O.H., 1981. Stratigraph and mineralogy of the manganese ores of Urucum. Mato Grosso, Brazil: Geologie Rundschau 70, 1077–1085.
Whitney, D.L., Evans, B.W., 2010. Abbreviaations for names of rock-forming minerals. Am. Mineral. 95 (1), 185–187. https://doi.org/10.2138/am.2010.3371.
Wignall, P.B., 1994. Black shales: Oxford. Clarendon Press, UK, pp. 124.
Wilson, D.E., 1980. Surface and complexation effects on the rate of Mn (II) oxidation in natural waters. Geochim. Cosmochim. Acta 44 (9), 1311–1317.
Young, G.M., 1976. Iron-formation and galciogenic rocks of the Rapitan Group, Northwest Territories, Canada. Precambr. Res. 3, 137–158.
Yu, W., Polgári, M., Gyollai, I., Fintor, K., Szabó, M., Kovács, I., Fekete, J., Yuansheng, Du.Y., Zhou, Q., 2019. Microbial metallogenesis of the Cryogenian manganese ore deposits in South China on micrometer scale. Precambr. Res. 322, 122–135.
Zwietering, M.H., Jongenburger, I., Rombouts, F.M., van Riet, T.K., 1990. Modeling of the bacterial growth curve. Appl. Envir. Microbiol. 56, 1875–1881.